NATIVE EARTH ELECTRIC FIELD MEASUREMENTS USING SMALL SPACECRAFT IN LOW EARTH ORBIT

by

John Pratt

A thesis submitted in partial fulfillment
of the requirements for the degree

of

MASTER OF SCIENCE

in

Electrical Engineering

Approved:

Dr. Charles M. Swenson Major Professor	Dr. Edmund A. Spencer Committee Member
Dr. Jacob Gunther Committee Member	Dr. R. Rees Fullmer Committee Member

Dr. Byron R. Burnham
Dean of Graduate Studies

UTAH STATE UNIVERSITY
Logan, Utah

2009

Abstract

Native Earth Electric Field Measurements Using Small Spacecraft in Low Earth Orbit

by

John Pratt, Master of Science

Utah State University, 2009

Major Professor: Dr. Charles M. Swenson
Department: Electrical and Computer Engineering

The use of small satellites to measure the native electric field of the earth has historically presented many problems as a result of the generally modest pointing capabilities of small satellites. In spite of this, the cost of small satellites makes them ideal for just such scientific missions. This thesis details many of the constraints of electric field measuring missions as well as the requirements on any spacecraft designed to accomplish such. The data from a small sounding rocket mission is then analyzed and its usefulness discussed. Possible other methods for use are also discussed.

(85 pages)

To my beautiful wife and our soon-to-be baby boy; my inspiration and driving force.
To my parents patient and kind, who have guided me for many years.
To a loving Father above, who was there in many a dark hour.

Acknowledgments

I wish to acknowledge those people whose help and support made this thesis a reality.

I am very grateful to Dr. Charles Swenson, for his many hours of work, instruction, and guidance for the work contained herein, as well as the effort he put into editing the final result. Also, I thank him for his inspiring classes which led me to this field of research.

I am indebted to Dr. Rees Fullmer and Dr. David Geller whose aid was invaluable throughout the chapter on Kalman filters and who never seemed to tire of my questions.

I would also like to thank Brian Bingham, co-worker and friend, who patiently explained the more subtle aspects of both Kalman filters and dynamics.

Finally, I express appreciation to Tyson Smith whose friendship meant the lightening of many endless hours of research as well as to all the many friends and fellow students who aided in many small ways.

John A. Pratt

Contents

List of Tables

List of Figures

Notation

Events

$\bar{x}$	x is a vector
$\hat{x}$	estimated value of x
$\tilde{x}$	measured value of x
$\bar{q}$	the vector component of the quaternion
q_4	the scalar component of the quaternion
Δx	the discrete time change in x from one time to another
δx	the error in an estimate of x
P_i	the covariance matrix of the variable i
$B_\otimes$	the cross product matrix of the vector B
$q_1 \otimes q_2$	the quaternion composition of q_1 and q_2

Acronyms

BFCS	body-fixed coordinate system
ECI	earth-centered inertial coordinate system
ECEF	earth-fixed, earth-centered coordinate system
rad/s	radians per second
Nm	Newton meter
IGRF	International Geomagnetic Reference Field
SPAS	SDL Pearl ADCS Simulation

Chapter 1

Introduction

1.1 Intent

From the earliest days of satellites one of the primary uses of spacecraft has been to increase our understanding of the earth and all regions of its atmosphere. The hopes of these missions has been to better understand the interaction of the atmosphere with our lives while simultaneously trying to decrease any adverse effects that may occur. The ionosphere has proven to be one of the most important regions of the atmosphere to analyze for our modern technological society.

The ionosphere consists of a region of the atmosphere stretching from 50 km to over 1000 km. The overall defining characteristic of this region is the ionized gases or plasmas which inhabit these regions. Solar radiation, as well as galactic cosmic rays, energize the atoms in this region allowing electrons to break free resulting in both ions and free electrons. The ratio of neutral and charged particles in the ionosphere fluctuates. This ratio is effected by time of day, season, solar cycles, and other factors [1–3].

Resulting from the pressure of the ionized gases are electric fields that shift with the movement of the gases. The electric effects in the ionosphere have both beneficial and harmful consequences. Among the beneficial consequences is the ability to bounce certain radio frequencies off the ionosphere allowing for long range radio communications. One of the harmful effects of the ionosphere is the noise induced in radio communications passing through these layers of the atmosphere. The ionization can cause both amplitude and phase modulation (known as scintillation) in any radio wave passing through it, although these effects can be decreased by using higher frequencies. The reduction of this noise is important to all classes of satellite communications. Other potential problems from electric fields arise in transmission lines and under sea cables, geophysical surveys, etc. [4].

The purpose of this thesis was inspired by a sounding rocket mission known as STORMS, given the NASA designation 36.218, and a desire to better understand the attitude knowledge requirements necessary to measure the electric field of the earth. It is hoped that the work and conclusions from this paper will make it easier to implement inexpensive and effective satellite missions for measuring the effects of the ionosphere, in particular the electric fields therein.

1.2 Background of the Thesis

1.2.1 STORMS Payload

In October of 2007 NASA launched rocket 36.218 carrying the mission entitled "Investigation of Mid-Latitude Ionospheric Irregularities Associated with Terrestrial Weather Systems" also known as the "STORMS Mission." The STORMS mission contained two payloads (see fig. 1.1). The main payload (or mother payload) instrumentation was constructed by the University of Texas Dallas and consisted of neutral wind and electric field measurements. The secondary payload (or daughter payload) was constructed by Utah State University/Space Dynamics Laboratory. The daughter payload contained various electron measurement instruments including four floating potential probes for measuring electric fields (see fig. 1.2). The payloads were launched to an altitude of approximately 450 km.

The purpose of the STORMS mission was to better understand the effect of large terrestrial weather events on the ionosphere and ionospheric anomalies and irregularities. In particular, the mission was designed to answer two questions: What is the cause of the spread in altitude of signatures of ionosonde (or dynasonde) observations of the reflection height of low-frequency radio waves? What effect does a large tropospheric weather system have on the density structures of the ionosphere above it [1]?

The mission report by NSROC released following the mission [5] highlights problems associated with the release of the daughter payload. According to flight data the motor finished de-spin at 54.2 seconds and then separated from the payloads at 56.2 seconds

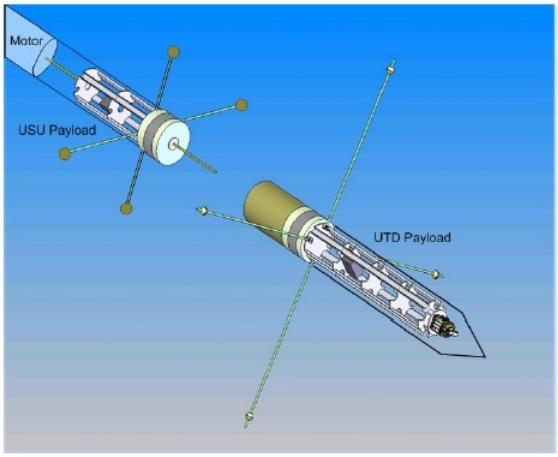

Fig. 1.1: The STORMS mission rocket payload configuration.

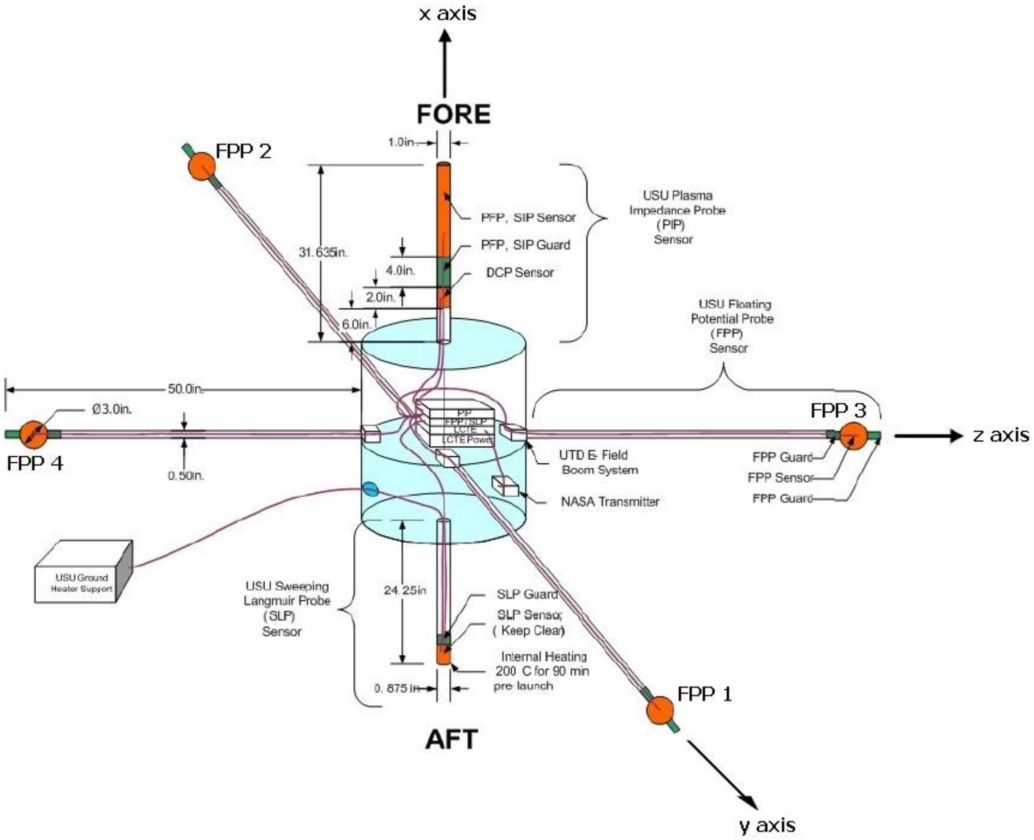

Fig. 1.2: The layout of the hardware and sensors on the daughter payload for the STORMS mission built by Utah State University and the Space Dynamics Laboratory.

after launch. The daughter booms started deployment after that and were fully deployed at 57.5 seconds. The daughter payload then separated from the other payload at 65.7 seconds. Approximately 42 seconds later the daughter payload experienced a sudden change in orientation, angular rates, and position and velocity relative to the mother payload. The magnetometer data shows an increase in roll rate of about 33% or from 0.7 Hz to 1.1 Hz. The magnetometer data collected is shown in fig. 1.3. Figure 1.4 shows the times highlighted above that effected the daughter payloads orientation and roll rate.

According to Disbrow [5] the coning exhibited by the spacecraft from 65 to 105 seconds is a result of an inertia ratio that is very close to one (or about 0.96 spin axis to transverse axis). Although this was predicted by pre-mission simulations the magnitude of the coning was unexpected.

The disturbance that took place at approximately 105 seconds has no certain origin. The mission report postulates that the disturbance was likely a result of a daughter-payload motor collision after release of the daughter payload from the mother payload. Even if this is the case, the reason for this collision is impossible to know, although residual thrust in the motor or variances in drag coefficients are raised as possible reasons. The purpose of this thesis, however, is not to determine what caused the disturbance but try to model the resulting spacecraft movement and extract the desired data.

1.2.2 Extracting the Electric Field Data

The electric field measured is dependent upon the cross product of the velocity and the magnetic field. This component, along with other error sources, must be removed from the measurement made by the floating potential probe in order to calculate the native electric field of the earth. As the magnetometer is fixed to the payload body the resulting measurements are in the body-fixed coordinate system. The velocity measurement, however, is a result of ground tracking of the spacecraft meaning that the velocity is in ECI coordinate system. Therefore, a large amount of the uncertainty in the electric field measurement can be the error in the rotation of the velocity vector to the body-fixed coordinate system in order to align it with the magnetometer and electric field data.

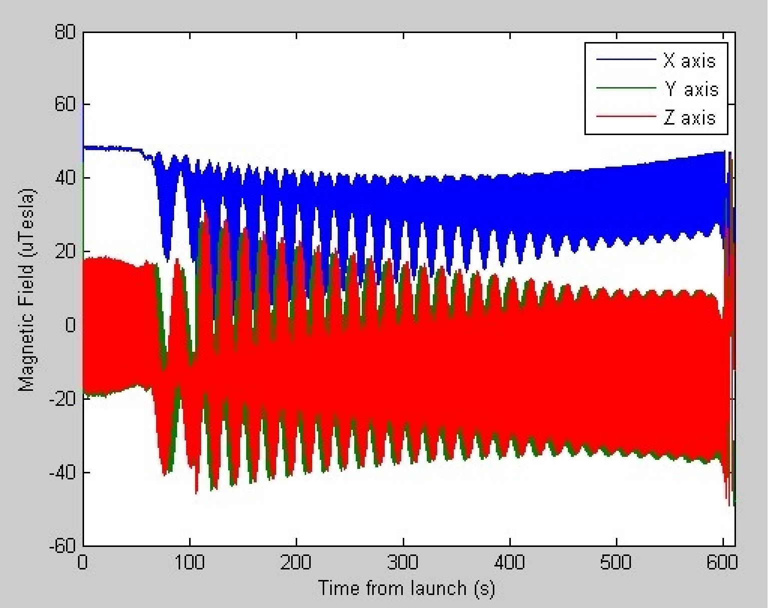

Fig. 1.3: Magnetic field data captured by STORMS payload.

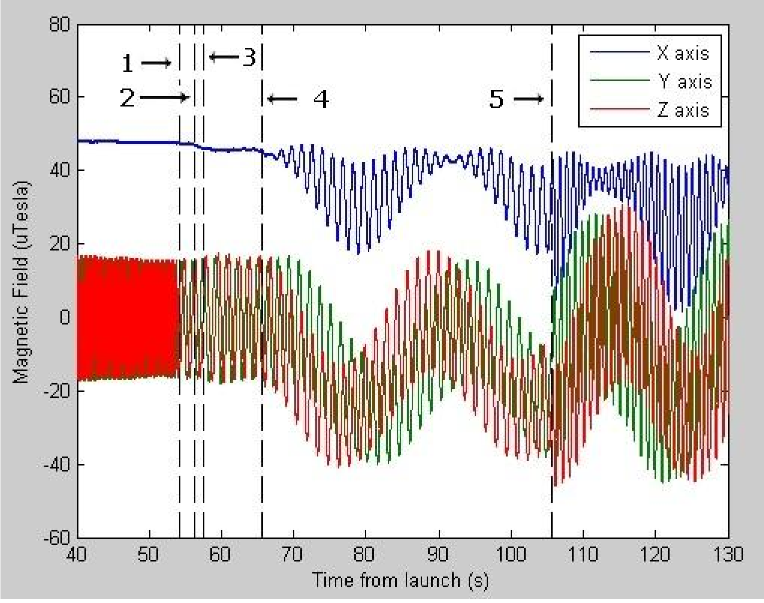

Fig. 1.4: Magnetic field data captured by the daughter payload on the storms mission. Black vertical lines highlight critical events during the flight including (from right to left): (1) motor de-spin, (2) motor separation, (3) daughter boom deployment, (4) daughter payload separation, and (5) an unknown event that caused dramatic changed.

In order to rotate the velocity into the body-fixed coordinate system the attitude of the spacecraft must be known. The only measurements available for measuring body attitude on the daughter payload were those from the magnetometer. Part of the work done for this thesis was the development of a Kalman filter to extract the spacecraft attitude from these measurements. A large part of the final error in the electric field scientific analysis will be a result of the error in the estimation of the body attitude.

Although the largest error associated with the electric field is a result of the velocity and magnetic field there are other errors that must be looked at to maximize the accuracy of the final electric field measurements. Accurately estimating and minimizing these errors will greatly improve the usefulness of this data.

1.2.3 Small Satellite Applications

One of the most important elements of this research is its effect upon possible small satellite missions which have had a goal to measure the electric field of the earth. The conclusions reached from the STORMS daughter payload data will provide answers to the following three questions:

How accurately must the attitude of the spacecraft be known?

How accurate must the measurements of the magnetic field be?

How accurate is the gathered electric field data?

With regards to a specific accuracy of measurement for the native electric field all three of these questions will be answerable. This will allow for the planning of such missions with justifiable confidence that the scientific goal is attainable and that the research money being spent is being used wisely.

A final by-product of this research will be the derivation of algorithms for analyzing like-mission data that can be used for future missions. These algorithms, while not universal, will be able to speed the time of understanding the result of missions for measuring the earth's environment.

1.3 Thesis Organization

This paper is organized into five chapters including the introduction. Chapter 2 details the working of electric field probes and their associated errors. It shows which errors are dominant and possible methods for decreasing there effect. The next chapter explains the derivation of the Kalman filter that has been used to analyze the STORMS data. The chapter also points out possible problems with this method and other approaches that might be taken to minimize these. The fourth chapter breaks down the results of applying the Kalman filter to the STORMS data and what can be said of the accuracy of these measurements. Chapter 5 contains the conclusion and consequences of this work.

Chapter 2

Electric Field Double Probes

2.1 Introduction

Langmuir probes are among the most versatile and simple of instruments used to collect information about the plasma environment [6, 7]. One of the many uses of these probes is the construction of the electric field double probe which consists of two Langmuir probes positioned along a line on opposing ends (see fig. 2.1). By comparing the relative potential of these two probes it is possible to infer the component of the electric field of the surrounding plasma in the direction of the probes. In this way it is possible for a spacecraft to measure the electric field of the atmosphere through which it passes.

Unfortunately, associated with measurements from electric field double probes are several possible sources for error. Many of these errors can be avoided or minimized through intelligent spacecraft design. Others can be measured with a high degree of accuracy and then removed from the measurements. This paper will explain the source of these different error sources, how they affect the measurement of the electric field, and what can be done to minimize their effect on the data. The code used for this analysis is included in Appendix A.

2.2 Workings of Electric Field Double Probes

2.2.1 Theory

Electric field double probes, as previously stated, are composed of two sensors mounted on opposite ends of a boom with instrumentation in the middle to measure the relative

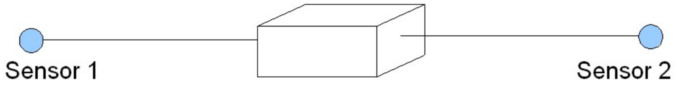

Fig. 2.1: Typical electric field double probe alignment.

potential. Ideally this simple instrument leads to the equation

$$\phi = \bar{E} \cdot \bar{d}, \tag{2.1}$$

where ϕ is the relative potential between the sensors, $\bar{E}$ is the electric field of the surrounding plasma, and $\bar{d}$ is the boom length and orientation upon which the sensors are mounted. There are, however, several assumptions which must be made in order to arrive at this simple formula and it is in analyzing these assumptions that the different sources of error in the data can be found.

One important assumption made in the formula above is that an electron will require the same energy to interact with sensor 1 as it will with sensor 2. This assumes that it takes the same energy for an electron to arrive at either sensor as well as it taking the same energy for an electron to enter or leave the surface of either sensor. In other words, it assumes that the sheath potential of the plasmas surrounding the two sensors are the same and that the work functions for both are the same (see fig. 2.2). As this is not always the case errors can arise in the data as a result of this assumption, and in secs. 2.2.3 and 2.2.4 these errors are looked at.

A key requirement of making a voltage measurement across an element is to insure that the measurement does not disturb the physics of what is occurring. This requires that the resistance of the meter be much greater than the resistance of the element being probed or, in other words, that the current drawn off by the measurement be small compared to the currents flowing in the system to be measured. The resistance of the system in the plasmas to be measured is known as the sheath resistance. The sheath resistance must be very small in comparison to the instrument resistance in order to minimize error. It is important to understand the necessary magnitude in order to do this and thus the resistance is looked

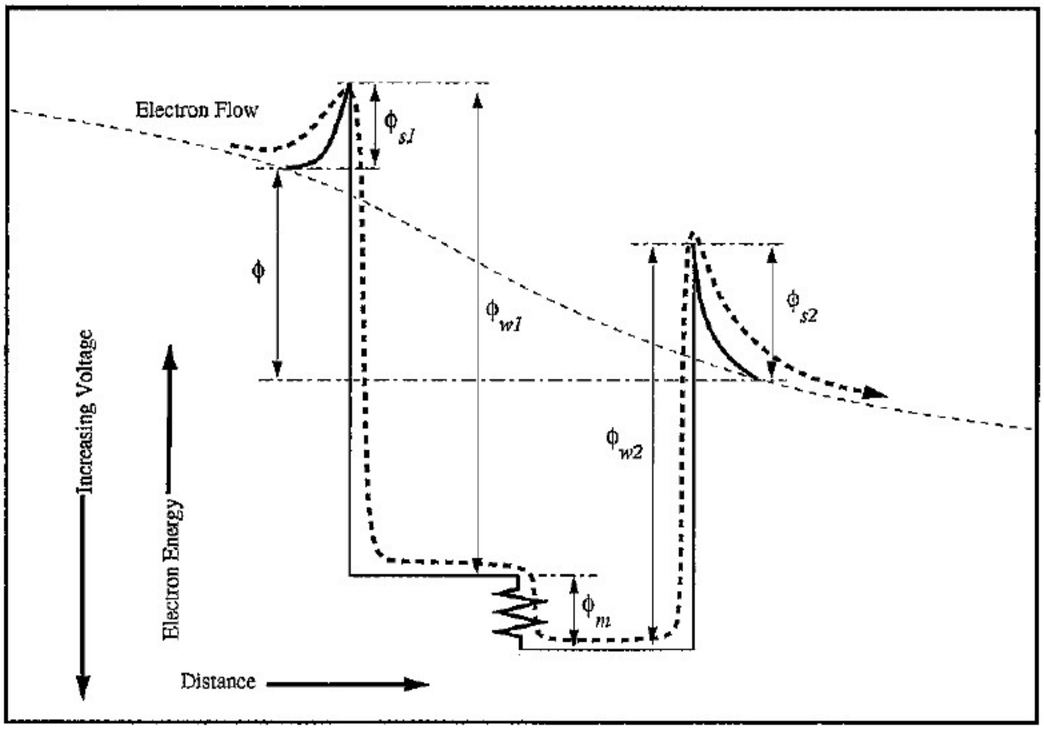

Fig. 2.2: Electron potential energy as a function of position near a double probe. Shows the relation between the measured electrical potential, the sheath potential of each probe, and the work function of each probe.

at in sec. 2.2.5.

One very important difference between the simple formula derived above and the actual measurements made is the fact that a spacecraft flying through the magnetic field of the earth will generate an electric field just due to this motion. As a result of the high velocity of the spacecraft, this electric field actually has a larger magnitude than the native electric field of the earth. The only way to compensate for this error is to be able to accurately estimate it and then remove it from the measurement. This is one of the most difficult tasks as well as being the largest error. This process is discussed in sec. 2.2.6.

A final error source is a result of the assumption that the separation vector, $\bar{d}$, between the sensors is known perfectly. The vector can be affected by both inaccurate construction/mounting of the boom as well as structural modes of the boom resulting in flexing or bowing. This can produce significant error as seen in sec. 2.2.7.

The final electric field double probe measurement formula is:

$$\phi = \frac{(\bar{E} + \bar{V} \times \bar{B}) \cdot (\bar{d} + \Delta d) + (\phi_{w1} - \phi_{w2}) + (\phi_{s2} - \phi_{s1})}{1 + \frac{R_{s_1}}{R_i} + \frac{R_{s_2}}{R_i}}, \tag{2.2}$$

where

ϕ_{si} is the sheath potential of the ith probe,

ϕ_{si} is the work function potential of the ith probe,

R_{s_i} is the sheath resistance of the ith probe,

R_i is the instrument resitance,

$\bar{V}$ is the spacecraft velocity vector,

$\bar{B}$ is the magnetic field around the spacecraft,

and d represents the boom the probes are mounted on.

Each of the terms helps to contribute to the noise on the measurement of the electric field, $\bar{E}$. A more detailed derivation of this formula can be found in papers by Gregory, Swenson, and Fahelson [1, 8–10].

2.2.2 Understanding the Figures in the Following Sections

For the most part, there are two types of figures used in sec. 2.2 in order to understand the magnitude of the errors associated with electric field probes. These figures are standard throughout this section, wherever that is possible, to aid in the comparison of one error source to another.

The first type of figure used is a simple error plot. This figure shows the size of an expected error in mV/m in the electric field measurement on the y-axis as a particular variable changes along the x-axis. The example electric field used for all these cases is 10 mV/m and total boom length of 10 m between the probes thus allowing for comparison against the generated error. For example, if a plot showed that a particular error varied from 0 to 1 mV/m then it would be understood that over the specified range the error was less than 10% of the example electric field. However, if the error ranged from 1 to 5 mV/m then the error source would be much more important to consider and minimize. Desired values for these plots would be as close to 0 as possible.

The second type of figure used is a signal to error plot which shows a ratio of the magnitude of the signal to the magnitude of the error. Once again an example electric field of magnitude 10 mV/m was used with a total boom length of 10 m between the probes. On the y-axis the signal to error ratio is shown while a particular variable changes along the x-axis over a specified range. For these figures, the desired value would be one as large as possible. Thus a value of 1 along the y-axis would indicate that the error was of equal strength to the signal while a value of 10 along the y-axis would indicate the error strength was only 10% of the strength of the signal. These plots are generally done with a logarithmic scale on the y-axis to ease understanding.

2.2.3 Sheath Potential Errors

The sheath potential for a Langmuir probe can be defined as

$$\phi_s = \frac{k_b T}{e} \ln\left(\frac{I_{other} - I_{i_{ram}}}{I_{e_{sat}}}\right).$$

I_{other} will have negligible difference between the two probes and therefore we assume it to be 0 in order to simplify. $I_{i_{ram}}$, the ion current swept out by the movement of the sensor, and $I_{e_{sat}}$, the electron saturation current, can be replaced using the formulas [9]

$$I_{e_{sat}} = -An_0 e\sqrt{\frac{k_b T_e}{2\pi m_e}}, \tag{2.3}$$

$$I_{i_{ram}} = A_c e n_0 V. \tag{2.4}$$

These two equations allow us to define the sheath potential only in terms of the plasma properties and probe properties. This results in the equation

$$\phi_{s1} - \phi_{s2} = \frac{k_b T_1}{e} \ln\left(\frac{A_c e n_1 V}{A n_1 e \sqrt{\frac{k_b T_1}{2\pi m_e}}} \right) - \frac{k_b T_2}{e} \ln\left(\frac{A_c e n_2 V}{A n_2 e \sqrt{\frac{k_b T_2}{2\pi m_e}}} \right), \tag{2.5}$$

$$= \frac{k_b T_1}{e} \ln\left(\frac{A_c V}{A \sqrt{\frac{k_b T_1}{2\pi m_e}}} \right) - \frac{k_b T_2}{e} \ln\left(\frac{A_c V}{A \sqrt{\frac{k_b T_2}{2\pi m_e}}} \right). \tag{2.6}$$

From the above equations we know that the following elements will be the same: V (the velocity), k_b (Boltzmann's contsant), e (electron potential), A (area of the probe), and m_e (mass of an electron). A_c, which is the cross-sectional area of a probe, will be the same for spherical probes. Cylindrical probes might have a slightly different cross-sectional area but only due to mounting errors. This should be so small that the resulting error is not important. Equation (2.6) can be simplified as

$$\phi_{s1} - \phi_{s2} = \alpha T_1 \ln(\frac{\beta}{\sqrt{T_1}}) - \alpha T_2 \ln(\frac{\beta}{\sqrt{T_2}}), \tag{2.7}$$

$$\text{where } \alpha = \frac{k_B}{e}$$

$$\text{and } \beta = \frac{A_c V}{A \sqrt{\frac{k_b}{2\pi m_e}}}.$$

As all terms in α and β are common to both the only remaining variable is the temperature of the plasma, T. It is also important to remember, however, that ϕ_s is actually the difference between the probe potential and the plasma potential. Therefore if the plasma potential varies from one point to another, this could lead to a serious error in the calculations.

As a result of variations in the plasma it is impossible to say that the two probes will be surrounded by plasma of the exact same properties. This problem is only exacerbated by the fact that boom lengths are typically very large (at least 6 meters) in order to achieve more accurate readings of the relatively small native earth electric field. However, the longer the boom lengths the less effect errors in the sheath potential have on the eventual estimate of $\bar{E}$. Therefore, some careful balancing must be done.

To test the effect of these parameters on an electric field measurement a simulation was constructed using the following parameters:

$$\begin{aligned} V &= 7.5 \;\; km/s, \\ r &= .01 \;\; m, \\ A &= 4\pi r^2 \;\; m^2, \\ \text{and } A_c &= \pi r^2 \;\; m^2. \end{aligned}$$

The temperature of probe one was set to 1300 Kelvin and the second probe was varied from 1300 to 1500 Kelvin; typical temperatures in the ionosphere. The difference between the two plasma potentials was varied from 0 to 0.05 volts. Figures 2.3 and 2.4 show the resulting error in the measured potential due to various differences in the temperature and plasma potential. It is important to note that these errors are in volts and that a typical electric field (about 10 mV/m) measured using 10 m booms would give a potential of .1 V. Therefore errors would generally need to be less than .01 V to keep the error under 10%.

From the figures it can be seen that a difference of more than 0.01 volts between the potential of the plasma surrounding the first probe and the plasma surrounding the second probe could lead to serious error in the resulting measurement. Also, a temperature difference of about 30 K would have the same effect. The two errors seem to add linearly.

2.2.4 Work Function Errors

The work function of a surface is the energy required for an electron at a surface to enter the surface. The work function for a particular material can vary depending on the

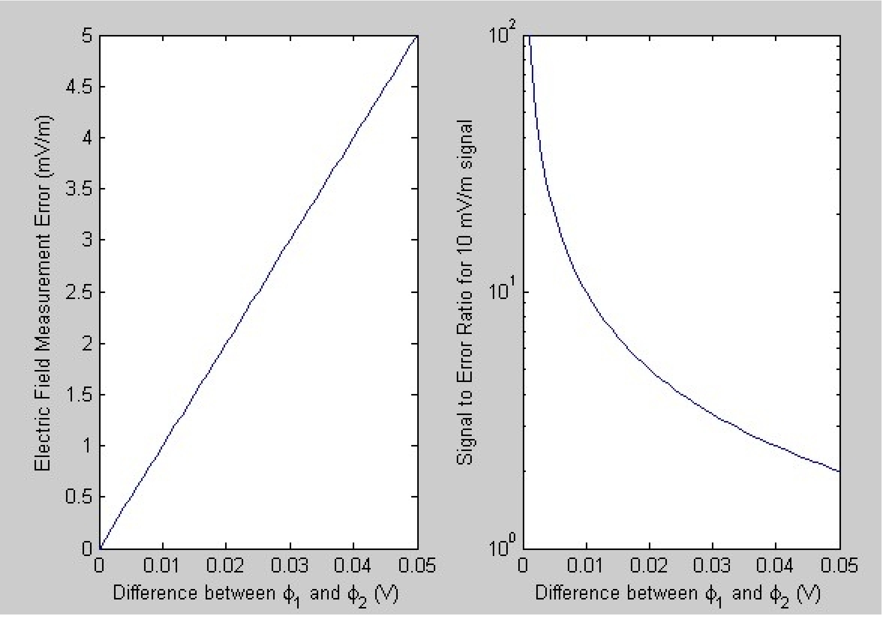

Fig. 2.3: Error in the electric field measurement due to variation in the differences between the two plasma potentials. The figure on the left shows the error as the difference in plasma potential varies from 0 V to 0.05 V. The figure on the right shows the signal-to-noise ratio for those errors with a 0.1 V signal.

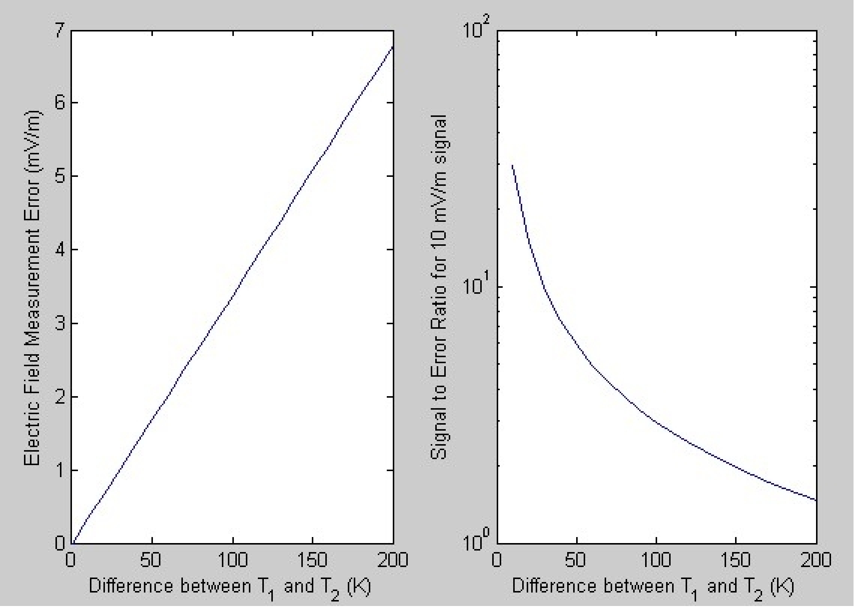

Fig. 2.4: Error in the electric field measurement due to variation in the differences between the two plasma temperatures surrounding the probes. The figure on the left shows the error as the difference in plasma temperatures varies from 0 K to 200 K. The figure on the right shows the signal-to-noise ratio for those errors with a signal of 0.1 V.

temperature of the material and how it was prepared. As long as both probes are prepared in the same manner, this ideally does not cause any problems.

The work function for a material, however, is not constant across a surface and can be approximated as a Gaussian function. The standard deviation for work function of materials typically used for building probes ranges from 1 mV to over 30 mV. Obviously there will be serious error in the measurements if the two probes have work functions that differ by 30 mV. Yet, in considering the grain size of the materials generally used, this turns out not to be a problem. All the materials typically used have grain sizes of 50 μm or less. Since the work function is Gaussian and a typical probe has a surface area of at least several square millimeters there turns out to be millions of grains in the surface of every probe and therefore, undoubtedly, the probe will be at the mean work function [11].

Although the average work function across the surface is constant, the real problem stems from the fact that the work function is not uniform across the surface. This problem generally arises as a result of surface contamination. Surface contamination can range anywhere from a fingerprint resulting from a careless touch during preparation to a layer of neutral gas particles acquired during flight. The difficulties and effects of surface contamination have been studied extensively, especially in regards to Langmuir probes, and are beyond the scope of this paper [6, 7].

A method frequently used to resolve issues with errors from the work function and sheath potential of electric field double probes is the spinning of the spacecraft. By rotating the spacecraft at a constant angular velocity the resulting electric field measurements are a sinusoid with a bias equal to the strength of the offsetting work potential and sheath potential error terms. This method allows for the disregarding of any difference in either. A slight problem with this method can arise from boom discrepancies explained in sec. 2.2.7.

2.2.5 Sheath Resistance Error

As shown in eq. (2.2) the resistance of the sheath between the probe and the plasma has a scaling effect upon the electric field measurement. For this reason neither the properties of the plasma, the boom length, or the difference in the probe properties has any effect upon this error. The only way to minimize this scaling effect is to have an instrument resistance large enough to cause the sheath resistance to be negligible.

The sheath resistance can be defined as [8]

$$R_s = \frac{\sqrt{2\pi m_e K_b T}}{A n_0 e^2} \exp(\frac{e\phi_s}{K_b T}). \tag{2.8}$$

Most of the terms in the equation are determined by the properties of the plasma and therefore are outside the control of the instrument designer. The variables that are possible to effect are A and ϕ_s or the area of the probe and the voltage of the probe relative to the plasma.

Typical values for this resistance can be found by picking a typical plasma condition at an altitude of 500 km. At this altitude likely values are T = 1300 K and $n_0 = 1e11$. K_b, e, and m_e are all constants. If we let $\alpha = \frac{\sqrt{2\pi m_e K_b T}}{n_0 e^2}$ and $\beta = \frac{e}{K_b T}$ then

$$\begin{aligned} R_s &= \frac{\alpha}{A} \exp(\beta\phi_s), \qquad (2.9) \\ &= \frac{125.17}{A} \exp(8.92\phi_s). \qquad (2.10) \end{aligned}$$

As the two probes used are very nearly identical in order to minimize the work potential error and the sheath potential error we can expect that R_1 and R_2 are very nearly equal (close enough to be a good approximation and not cause any additional errors). The electric field with sheath resistance separated can be defined as (if all other errors are set to 0)

$$\phi = \bar{E} \cdot \bar{d} - \frac{2R_s(\bar{E} \cdot \bar{d})}{R + 2R_s}. \tag{2.11}$$

The error due to the sheath resistance will then be

$$E_{sr} = \frac{2R_s(\bar{E} \cdot \bar{d})}{R + 2R_s}. \tag{2.12}$$

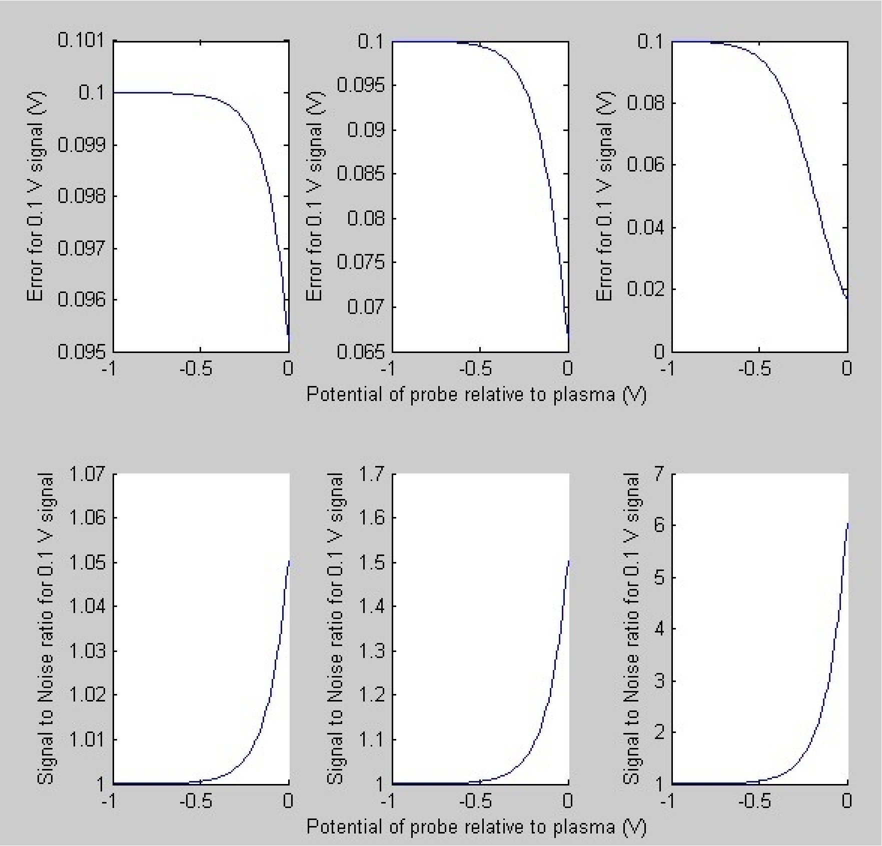

Fig. 2.5: Error in the electric field measurement as a result of a nonzero sheath resistance. The x-axis varies the probe potential relative to the plasma from -1 V to 0 V. The top figures show the error when the radius of the spherical probe is 1 mm. The bottom figures show the corresponding signal-to-noise ratio. The instrument resistance varies for the three as: 10^6 (left), 10^7 (center), 10^8 (right) ohms.

Using eqs. (2.9) and (2.12) a simulation was run to compute the magnitude of the error resulting (a value of 0.1V was used for $\bar{E} \cdot \bar{d}$). The results are shown in figs. 2.5 and 2.6. From these figures it can be seen that the most important thing with regards to this error is making the instrument resistance sufficiently large. If this is done the sheath resistance can be ignored.

2.2.6 Magnetically Generated Electric Field Error

A spacecraft flying in low earth orbit will have a velocity of about 7.5 km/s. At that altitude the strength of the earth magnetic field ranges from about 20,000 to 50,000 nT. This results in a generated electric field of about 100 mV/m (see fig. 2.7). If the electric

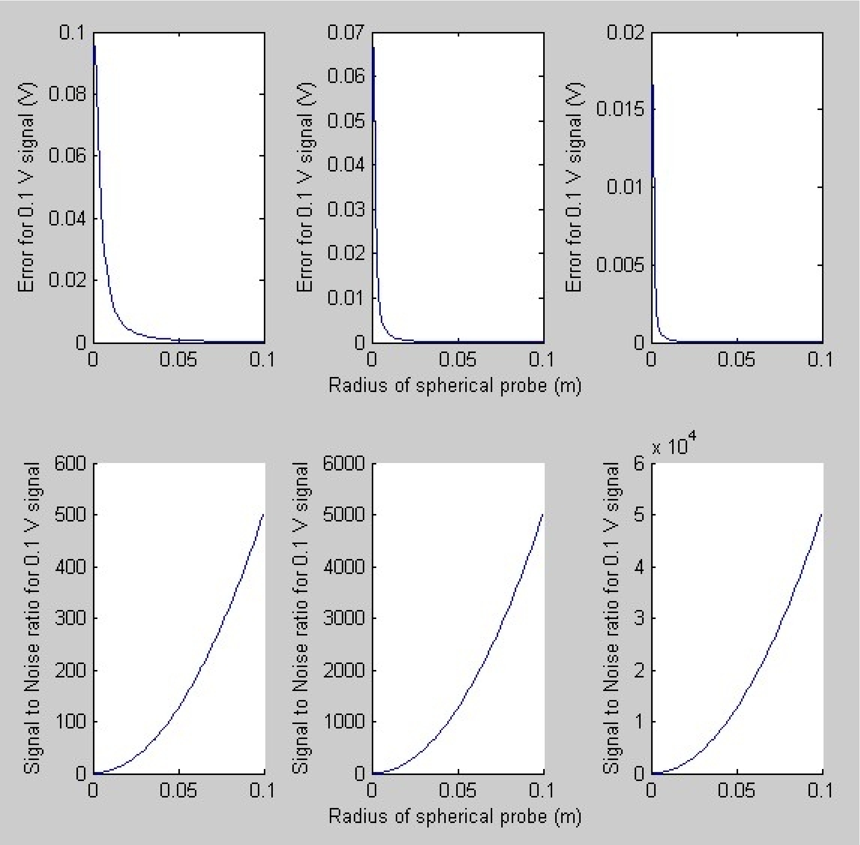

Fig. 2.6: Error in the electric field measurement as a result of a nonzero sheath resistance. The x-axis varies the probe potential relative to the plasma from -1 V to 0 V. The top figures show the error when the probe potential with respect to the plasma potential is 0V. The bottom figures show the corresponding signal-to-noise ratio. The spherical probe radius is varied on the x-axis. The instrument resistance varies for the three as: 10^6 (left), 10^7 (center), 10^8 (right) ohms.

field of the earth is about 10 mV/m, then the generated electric field is about one order of magnitude larger than the native earth electric field. This leads to some serious problems in deciphering data collected by the electric field double probe.

In order to compensate for the generated electric field we adjust the electric field measurement (after minimizing all the other errors) by using the formula $E = E_m - V \times B$ where E_m is the measurement of the instrument. This equation, however, means that errors in the measurement of the velocity, V, and the magnetic field, B, will continue through into the calculation of the electric field, E. If we define a state vector $X = \begin{bmatrix} V \\ B \end{bmatrix}$ and let P_i

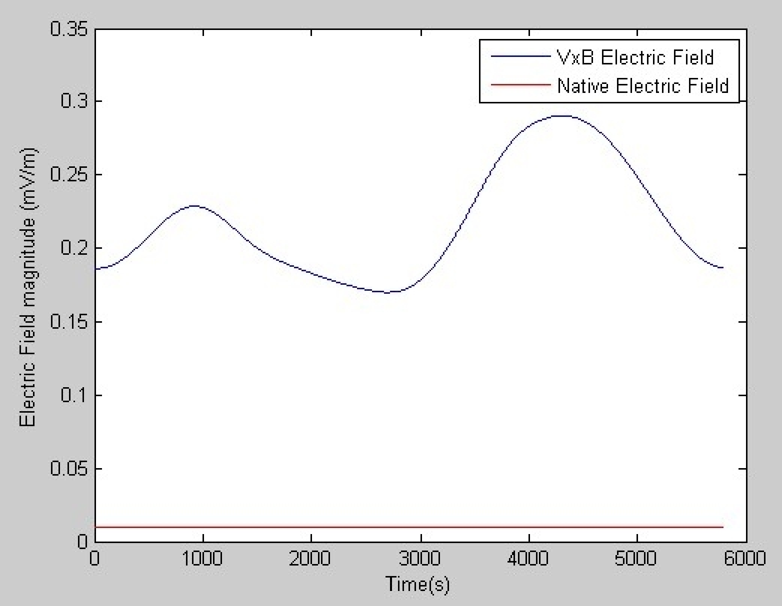

Fig. 2.7: Typical electric fields experienced in a low earth orbit. The blue line is the VxB electric field while the red line shows a typical ambient electric field.

represent the covariance matrix for a variable i then the covariance matrix of the electric field can be found as follows:

$$\begin{aligned}
&P_E = P_{Em} + P_{V\times B}, \text{ where}\\
&P_{Em}, \text{ the covariance of the electric field measurement}\\
&\quad \text{comes from the instrument specs, and}\\
P_{V\times B} &= \frac{d(V\times B)}{dX} P_X \frac{d(V\times B)}{dX}^T\\
&= \begin{bmatrix} -B_\otimes & V_\otimes \end{bmatrix} \begin{bmatrix} P_V & 0 \\ 0 & P_B \end{bmatrix} \begin{bmatrix} -B_\otimes^T \\ V_\otimes^T \end{bmatrix}\\
&= B_\otimes P_V B_\otimes^T + V_\otimes P_B V_\otimes^T \quad .
\end{aligned} \tag{2.13}$$

This is only true if the noise on the electric field measurement is uncorrelated with the noise on the magnetic field and velocity measurements.

If we assume that the electric field measurement, the magnetic field measurement and the velocity measurement are in the same coordinate frame (a poor assumption as will be discussed further in the section), then the only error comes from inaccuracies in the instruments used. Spacecraft attitude magnetometers are generally accurate to within about 10 nT and velocity can easily be found using GPS to within 10 cm/s. Figures 2.8 and 2.9 shows the typical expected error as a result of these inaccuracies.

The electric field measurement and magnetometer measurement are actually in the spacecraft body coordinate frame. As the velocity is typically obtained using GPS it is in the earth inertial frame or earth fixed frame. This means that there are two possible misalignments: one as a result of an offset during the mounting of the magnetometer causing errors in the magnetic field measurement, the other stemming from an inaccurate transformation from the earth frame (the typical frame for velocities) to the body frame (in which we have all the measurement data). In actuality these two errors will look like the same error for the most part and thus are treated the same here.

For coordinate transformations euler angles are frequently used. For small angles it can be shown via the small angle approximation of sines and cosines [12] that the transformation

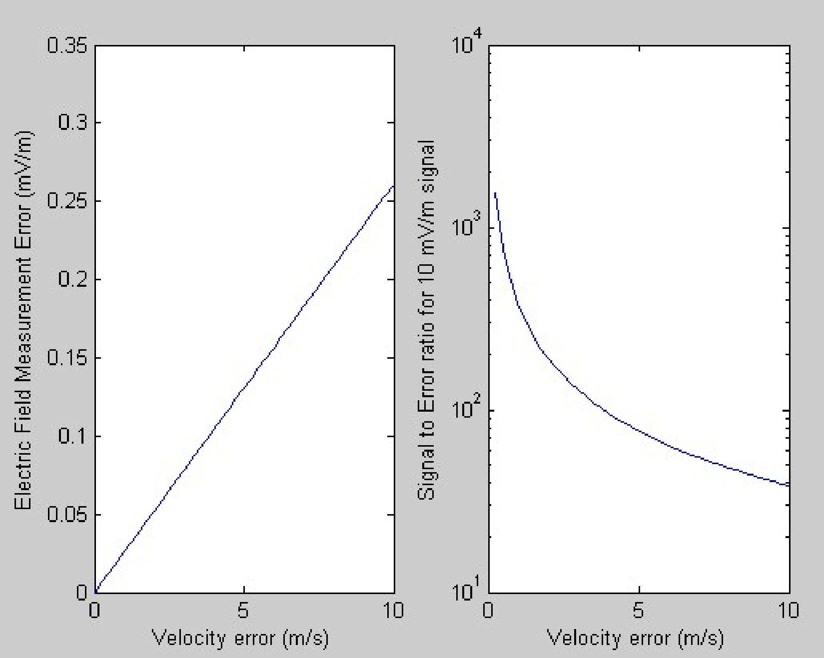

Fig. 2.8: Errors in the electric field measurement as a result of inaccuracies in the measurements of the velocity (left) and the corresponding signal-to-noise ratio (right). The velocity errors are varied on the x-axis from 0 to 100 m/s. The earth electric field used is 10 mV/m.

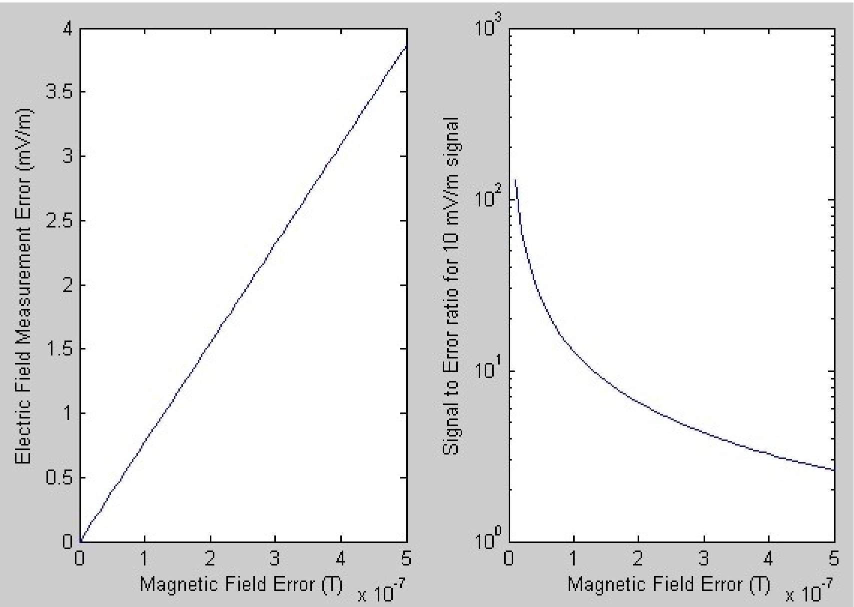

Fig. 2.9: Errors in the electric field measurement as a result of inaccuracies in the measurements of the magnetic field (left) and the corresponding signal-to-noise ratio (right). The magnetic field errors are varied on the x-axis from 0 to 1 microtesla. The earth electric field used is 10 mV/m.

matrix from one coordinate system to another can be described as

$$\Re = \begin{bmatrix} 1 & \psi & -\theta \\ -\psi & 1 & \phi \\ \theta & -\phi & 1, \end{bmatrix} \tag{2.14}$$

where ϕ is the variation on the x-axis, θ is the variation on the y-axis, and ψ is the variation on the z-axis [12]. Therefore, $\tilde{V} = \Re_e * \Re * V$ where V is the true velocity in the inertial frame, $\tilde{V}$ is the measured velocity in the body frame, $\Re$ is the true transformation matrix from inertial to body, and $\Re_e$ is the error associated with our transformation. The error in the electric field measurement can then be found by simply finding the difference between the true V cross B term and the V cross B term using $\tilde{V}$.

The desired frame for the final electric field will be the earth fixed frame or earth inertial frame as the spacecraft body frame is relatively useless. This means that the transformation matrix calculated will need to be used twice: once to transform the inertial velocity into velocity in the body frame and a second time to transform the native earth electric field in body frame to the electric field in inertial frame. However, as the electric field derived from the velocity and magnetic field terms is an order of magnitude higher than the actual electric field, the errors associated with the first transformation will be an order of magnitude higher than the errors associated with the second. For this reason the second set were ignored in the model.

A Monte Carlo simulation was developed to test the magnitude of resulting errors depending on the strength of the input errors. The simulation generates velocity and magnetic field for a nearly circular orbit at an altitude of 600 km and an inclination of 20 degrees. The velocity is derived using a basic gravity model. The magnetic field comes from the IGRF magnetic model using 2007 as the time of the orbit.

In fig. 2.10 the mean electric field error is shown with standard deviation as the attitude error increases. It can be seen that if the attitude error is kept down to about 0.2 degrees the electric field error is sufficiently small as long as the earth electric field is on the order of 10 mV/m (see fig. 2.11). When the rotation error reaches 1 degree standard deviation there is enough error in the electric field measurement that it is almost unusable. Thus, it is very important for an accurate understanding of the attitude of the spacecraft.

2.2.7 Boom Errors

Both errors in the length of the boom and errors of the alignment of the boom can cause problems in the measurement of the electric field. If a coordinate system is created such that the boom is mounted along the x-axis ($\bar{d} = \begin{bmatrix} d & 0 & 0 \end{bmatrix}^T$) then the actual boom can be modeled as

$$\bar{d}' = \begin{bmatrix} \sqrt{(d+\delta d)^2 - \delta y^2 - \delta z^2} \\ \delta y \\ \delta z \end{bmatrix}, \tag{2.15}$$

where δd is the error in the length of the boom, and δy and δz are errors in the alignment of the boom.

These errors are not only a result of possible misconstruction but more likely a result

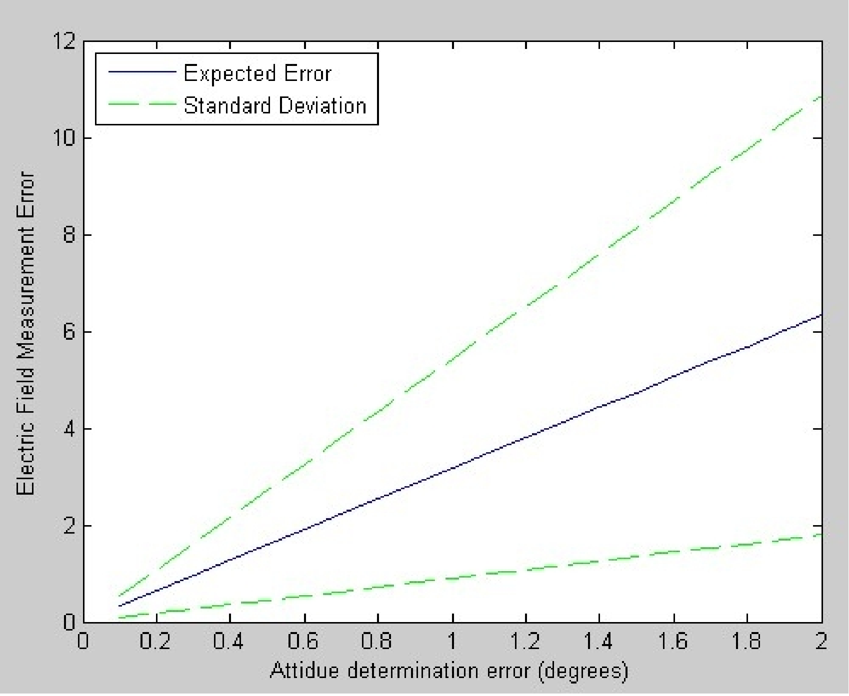

Fig. 2.10: Expected electric field measurement error with the corresponding 3-σ standard deviation for attitude errors varying from 0 to 2 degrees.

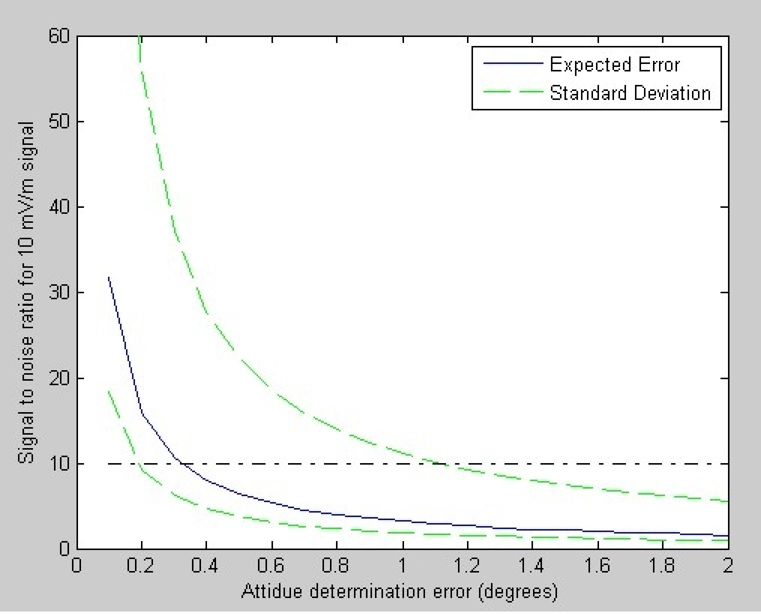

Fig. 2.11: Expected signal-to-noise ratio for the error associated with the velocity induced electric field. The x-axis shows the standard deviation of the attitude error for a specific Monte Carlo analysis. The y-axis is the mean signal-to-noise ratio for each analysis. The green bounds are the standard deviation.

of bowing or flexing of the booms during flight. As a result of the length of the booms they are very susceptible to distortion. Depending upon the natural modes of the booms the resulting distortion could effect the electric field measurements significantly.

These errors will cause two inaccuracies in the electric field measurements. The first error will be an incorrect measurement of the amplitude of a spinning electric field double probe. The second error will be an incorrect offset of the wave. The errors can be approximated as

$$\Delta E = \frac{|E \cdot \bar{d} - E \cdot \bar{d}'|}{d}. \tag{2.16}$$

Although this error when simulated is not exact because of the complexity of electric fields it will allow for a good comparison to the other errors modeled in this paper. These errors were modeled in Matlab for possible changes in δd, δy, and δz. For the simulation $\delta y = \delta z$. Figures 2.12 and 2.13 show some of the possible errors. These figures show that for the most part the error resulting from inaccuracies in the boom length is extremely small when compared to a 10 mV/m electric field and will most likely not affect the final measurement of the electric field enough to factor into the design considerations.

2.3 Results of Electric Field Probe Error Analysis

Although relatively large errors may be generated from the sheath potential and work potential, correction for these errors can be found be rotating the spacecraft. The sheath resistance errors can also be large unless a sufficient resistor is used in the instrument. The inaccuracies in the boom length can cause errors but they seem to be small in comparison to most of the others. The misalignment in the transformation of the velocity from inertial frame to body frame seems to be the largest error that is difficult to correct. In order to avoid this, a highly accurate knowledge of the attitude of the spacecraft is required. This could affect the cost and size of potential spacecraft for use in measuring the earth electric field.

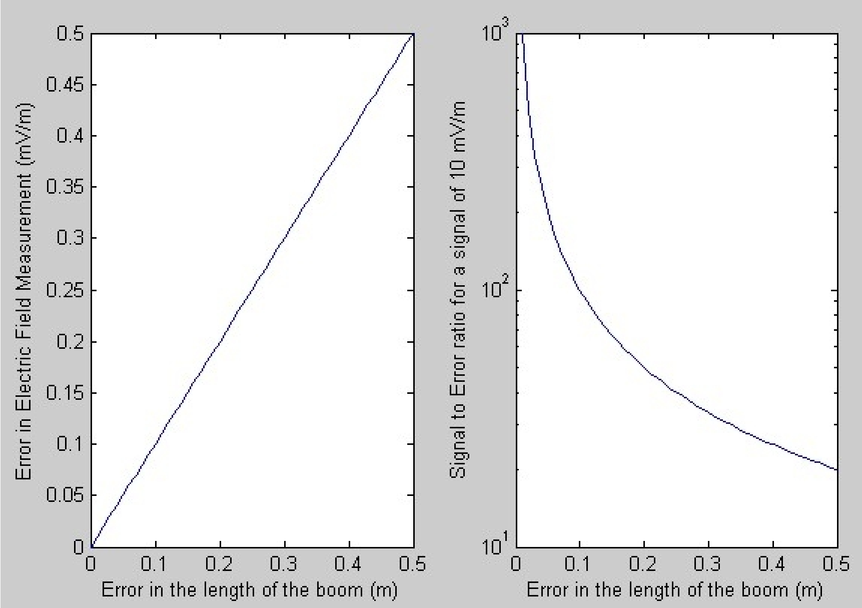

Fig. 2.12: Error in the electric field measurement as a result of inaccuracies in the boom length. The error is shown in the left figure while the signal-to-noise ratio is shown in the right. Boom length error varies on the x-axis from 0 to 1 mm. An electric field of 10 mV/m was used.

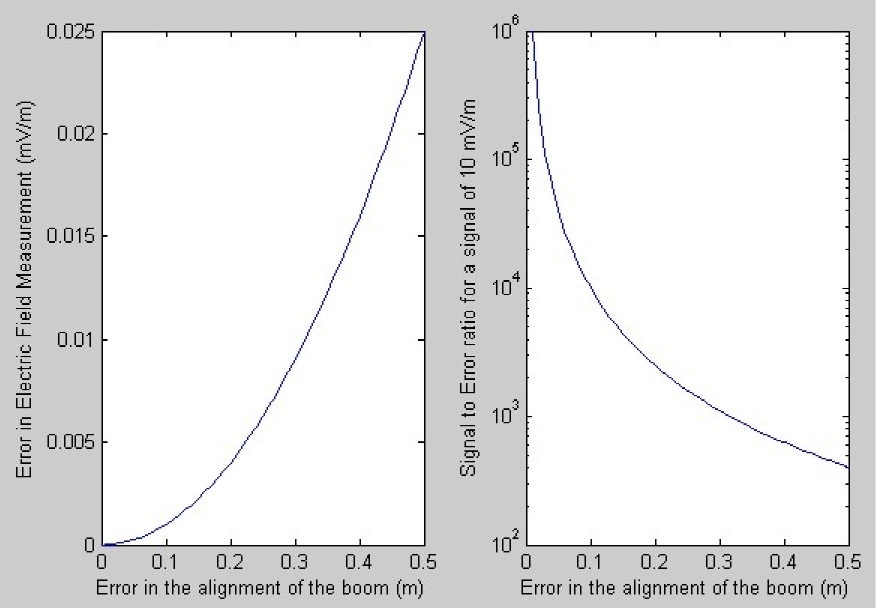

Fig. 2.13: Error in the electric field measurement as a result of inaccuracies in the boom alignment. The error is shown in the left figure while the signal-to-noise ratio is shown in the right. Boom length misalignment varies on the x-axis from 0 to 10 mm. An electric field of 10 mV/m was used.

The STORMS daughter payload was spun in order to mitigate the sheath and work functions errors as explained. However, because of the coning some of this advantage is lost in the difficulty of interpreting the final data results. Still, the largest errors are the inaccuracies as a result of the pointing of the spacecraft being uncertain. This is shown in the next two chapters.

Chapter 3

Derivation and Testing of the Kalman Filter

3.1 Introduction

Among the most reliable methods for the analysis of the attitude of a spacecraft is the extended Kalman filter. The extended Kalman filter makes use of both the linear and nonlinear equations in order to maximize its accuracy and speed. For the determination of the attitude of the daughter payload from the STORMS mission it was determined that the best method would be the use of an extended Kalman filter. This section discusses the derivation of such a filter for use with magnetometer-only attitude determination which can present unique challenges. Also explored in this section is the accuracy with which the derived filter can predict the attitude of the spacecraft. The code developed for this section is in Appendix C.

The derivation in this chapter relied heavily on work by several authors in particular Todd Humphreys [13, 14] and Mark Psiaki [14–16]. Notable work on extended Kalman filters was obtained from Crassidis [17] as well as many common terms used to describe these filters.

3.2 SDL Pearl ADCS Simulation

Throughout this chapter the SDL Pearl ADCS Simulation (referred to as the SPAS) is used to verify and understand the results produced by the Kalman filter. The SPAS is a model developed by Dr. Rees Fullmer and Bryan Bingham that incorporates high-level dynamic and sensor models to accurately simulate data for a satellite in various orbits. The model is able to provide to the user orbital data at any point as well as the expected reading that on-board sensors would provide. The noise associated with any of these measurements is adjustable according to the preference of the user. The SPAS code is in Appendix D.

3.3 Derivation of State and State Propagation

The state model for the attitude of the spacecraft to be used is going to include three different vectors. The state is defined as

$$x = \begin{bmatrix} q \\ \bar{\omega} \\ \bar{n}_d \end{bmatrix}, \tag{3.1}$$

where q is the earth-centered-inertial to body-fixed four element quaternion, $\bar{\omega}$ is the angular velocity of the probe relative to the inertial frame but expressed in body coordinates, and $\bar{n}_d$ is the disturbance torque on the probe in the body frame. The complete state space model for use with the Kalman filter is

$$\dot{x} = Fx + G\omega, \tag{3.2}$$

$$y = Hx + \eta. \tag{3.3}$$

In eq. (3.2) x represents the state, ω represents the process or system noise, and F and G represents matrices that relate the respective variables to the change in the state. In eq. (3.3) H represents the measurement sensitivity matrix and η represents the measurement noise. As the state equations are nonlinear an extended Kalman filter is used to obtain the most accurate results possible. This means that, although linear assumptions are made in order to propagate the covariance matrix, the full nonlinear state equations will be used to propagate the states.

Hence, in order to develop the extended Kalman filter it is necessary to have the rate of change of all the variables in the state. As the external torque is mostly just noise and varies slowly in the inertial frame it can be said that the disturbance torque in the inertial frame, $\dot{\bar{n}}_{d_I} \approx 0$. It then follows, using A as the rotation matrix from inertial to body coordinates and using $\dot{A} = -[\omega\times]A$ from Crassidis [17], that

$$\dot{\bar{n}}_d = \frac{d}{dt} A\bar{n}_{d_I}, \tag{3.4}$$

$$= \dot{A}\bar{n}_{d_I} + A\dot{\bar{n}}_{d_I}, \tag{3.5}$$

$$= -[\bar{\omega}\times]A\bar{n}_{d_I}, \tag{3.6}$$

$$= -[\bar{\omega}\times]\bar{n}_d, \tag{3.7}$$

$$= \bar{n}_d \times \bar{\omega}. \tag{3.8}$$

The rotation matrix, A, is defined in relation to the quaternion to be [12]

$$A = \begin{bmatrix} q_1^2 - q_2^2 - q_3^2 + q_4^2 & 2(q_1q_2 + q_3q_4) & 2(q_1q_3 - q_2q_4) \\ 2(q_1q_2 - q_3q_4) & -q_1^2 + q_2^2 - q_3^2 + q_4^2 & 2(q_2q_3 + q_1q_4) \\ 2(q_1q_3 + q_2q_4) & 2(q_2q_3 - q_1q_4) & -q_1^2 - q_2^2 + q_3^2 + q_4^2 \end{bmatrix}. \tag{3.9}$$

The quaternion rate of change is also defined by Sidi [12] and Crassidis [17]. It is shown to be

$$\dot{q} = \frac{1}{2}\Omega(\bar{\omega})q, \tag{3.10}$$

$$= \frac{1}{2}\begin{bmatrix} -[\bar{\omega}\times] & \bar{\omega} \\ -\bar{\omega}^T & 0 \end{bmatrix} q, \tag{3.11}$$

$$= \frac{1}{2}\begin{bmatrix} 0 & \omega_3 & -\omega_2 & \omega_1 \\ -\omega_3 & 0 & \omega_1 & \omega_2, \\ \omega_2 & -\omega_1 & 0 & \omega_3 \\ -\omega_1 & -\omega_2 & -\omega_3 & 0 \end{bmatrix} q. \tag{3.12}$$

The matrix in (3.12) can be recognized as the quaternion multiplication matrix. Therefore, if we define a new quaternion as

$$q_w = \begin{bmatrix} \bar{\omega} \\ 0 \end{bmatrix}, \tag{3.13}$$

then eq. (3.10) can be rewritten using quaternion composition as

$$\dot{q} = \frac{1}{2} q_\omega \otimes q. \tag{3.14}$$

Also from Crassidis [17] the rate of change for the angular velocity is described as

$$\dot{\bar{\omega}} = J^{-1}(-[\bar{\omega}\times]J\bar{\omega} + \bar{n}), \tag{3.15}$$

where J is the spacecraft inertia matrix (J being used instead of I in order to avoid confusion with the identity matrix) and $\bar{n}$ is the summation of all torques in the body frame. This equation holds as long as there are no momentum wheels on board the spacecraft. If there are no control torques present then the only torques influencing the system are the body torques meaning $\bar{n} = \bar{n}_d$.

Using the rates of change determined above the state can be propagated using integration over small intervals. A simulation in MatLab was created to do this. The integration implemented was a Runga-Kutta 4th order method. The simulation was tested against the SPAS. The comparison in figs. 3.1, 3.2, and 3.3 show that the propagation of the state can be done to a very accurate degree.

3.4 Derivation of Covariance Matrix Propagation

In order to propagate the covariance matrix it is necessary to use the error in the linearized versions of the state equations (i.e. δq, the difference between the state estimate and the true state, instead of $\hat{q}$, the state estimate). This helps especially in avoiding any coupling issues with the quaternion state (the four elements of the quaternion are not independent).

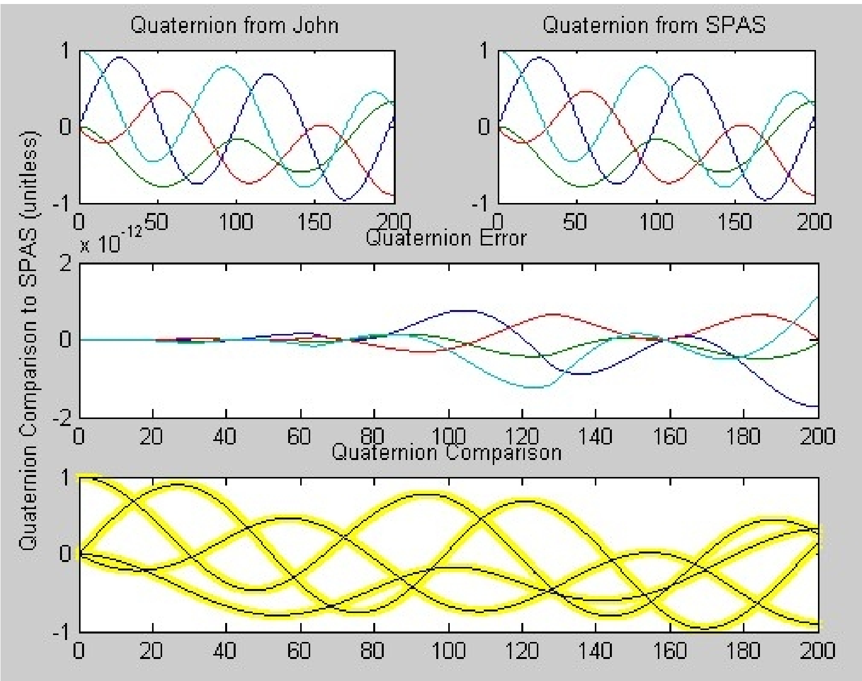

Fig. 3.1: Comparison of the derived quaternion propagation with known good data. Error results, shown in the middle graph, are on the order of 10^{-12}. The bottom graph shows the comparison of the SPAS data (yellow) with the Kalman filter integration (black). Quaternions are unitless.

The derivation of the linearized quaternion equations is followed in Crassidis [17]. This derivation yields the result:

$$\delta\dot{q} = -\begin{bmatrix} [\hat{\bar{\omega}}\times]\delta\bar{q} \\ 0 \end{bmatrix} + \frac{1}{2}\begin{bmatrix} \delta\bar{\omega} \\ 0 \end{bmatrix} \otimes \delta q. \tag{3.16}$$

From (3.16) the δq_4 state is seen to be 0. For this reason the error in q_4 can be dropped from the covariance propagation which only leaves three noncoupled elements. The covariance matrix for the state is then based on the vector portion of the quaternion, $\delta\bar{q}$, and not the full quaternion, δq.

$$\delta\dot{\bar{q}} = -[\hat{\bar{\omega}}\times]\delta\bar{q} + \frac{1}{2}\delta\bar{\omega} \tag{3.17}$$

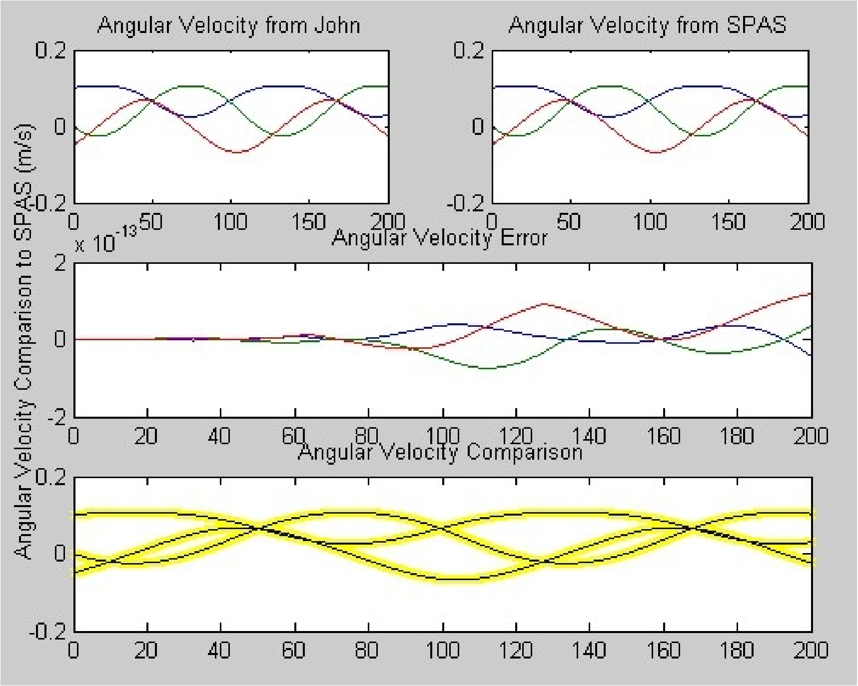

Fig. 3.2: Comparison of the derived angular velocity propagation with known good data. Error results, shown in the middle graph, are on the order of 10^{-13}. The bottom graph shows the comparison of the SPAS data (yellow) with the Kalman filter integration (black).

To use this for the propagation of the covariance matrix it is necessary to know the rate of change of the quaternion with respect to the state as shown below.

$$\frac{d\delta\dot{\bar{q}}}{d\delta X} = \begin{bmatrix} \frac{d\delta\dot{\bar{q}}}{d\delta\bar{q}} & \frac{d\delta\dot{\bar{q}}}{d\delta\bar{\omega}} & \frac{d\delta\dot{\bar{q}}}{d\delta\bar{n}_d} \end{bmatrix}, \tag{3.18}$$

$$= \begin{bmatrix} -[\hat{\bar{\omega}}\times] & \frac{1}{2}I_{3x3} & 0_{3x3} \end{bmatrix}. \tag{3.19}$$

Next we find the linearized version of $\delta\omega$. This is done by using the substitution $\bar{\omega} = \hat{\bar{\omega}} + \delta\bar{w}$ and $\bar{n}_d = \hat{\bar{n}}_d + \delta\bar{n}_d$. The linearized version of the angular velocity is then shown to be

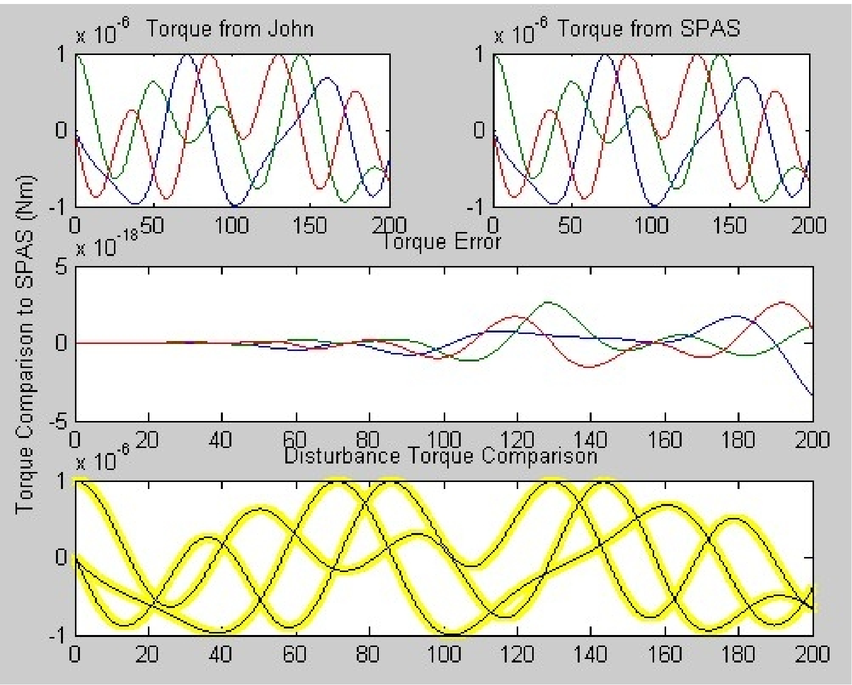

Fig. 3.3: Comparison of the derived torque propagation with known good data. Error results, shown in the middle graph, are on the order of 10^{-18}. The bottom graph shows the comparison of the SPAS data (yellow) with the Kalman filter integration (black).

$$\delta\dot{\omega} = \dot{\bar{\omega}} - \dot{\hat{\omega}}, \tag{3.20}$$

$$= J^{-1}(-[\bar{\omega}\times]J\bar{\omega} + \bar{n}_d) - J^{-1}(-[\hat{\omega}\times]J\hat{\omega} + \hat{n}_d), \tag{3.21}$$

$$= J^{-1}\delta n_d - J^{-1}([\bar{\omega}\times]J\bar{\omega} - [\hat{\omega}\times]J\hat{\omega}), \tag{3.22}$$

$$= J^{-1}\delta n_d + J^{-1}(J\delta\omega \times \delta\omega + J\hat{\omega} \times \delta\omega + J\delta\omega \times \hat{\omega}). \tag{3.23}$$

The derivative of (3.23) with respect to the error in the states is

$$\frac{d\delta\dot{\omega}}{d\delta X} = \begin{bmatrix} \frac{d\delta\dot{\omega}}{d\delta\bar{q}} & \frac{d\delta\dot{\omega}}{d\delta\bar{\omega}} & \frac{d\delta\dot{\omega}}{d\delta\bar{n}_d} \end{bmatrix}, \tag{3.24}$$

$$= \begin{bmatrix} 0_{3x3} & J^{-1}([J\hat{\omega}\times] - [\hat{\omega}\times]J + [J\delta\omega\times] - [\delta\omega\times]J) & J^{-1} \end{bmatrix}. \tag{3.25}$$

In (3.25) the value of $\delta\omega$ will be unknown which causes a potential problem. However, $\delta\omega$ should be much, much smaller than $\hat{\omega}$, therefore it can be assumed to be nearly zero. This allows for the exclusion of the terms which depend on $\delta\omega$ resulting in the final equation:

$$\frac{d\delta\dot{\bar{\omega}}}{d\delta X} = \begin{bmatrix} 0_{3x3} & J^{-1}([J\hat{\bar{\omega}}\times] - [\hat{\bar{\omega}}\times]J) & J^{-1} \end{bmatrix}. \tag{3.26}$$

Finally, the linearized version of $\bar{n}_d$ is found by applying the assumptions $\bar{\omega} = \hat{\bar{\omega}} + \delta\bar{\varpi}$ and $\bar{n}_d = \hat{\bar{n}}_d + \delta\bar{n}_d$ to (3.8):

$$\begin{aligned} \delta\dot{n}_d &= \dot{\bar{n}}_d - \dot{\hat{\bar{n}}}_d, && (3.27)\\ &= \bar{n}_d \times \bar{\omega} - \hat{\bar{n}}_d \times \hat{\bar{\omega}}, && (3.28)\\ &= (\hat{\bar{n}}_d + \delta\bar{n}_d) \times (\delta\bar{\varpi} + \hat{\bar{\omega}}) - \hat{\bar{n}}_d \times \hat{\bar{\omega}}, && (3.29)\\ &= \hat{\bar{n}}_d \times \delta\bar{\varpi} + \delta\bar{n}_d \times \hat{\bar{\omega}} + \delta\bar{n}_d \times \delta\bar{\varpi}. && (3.30) \end{aligned}$$

Taking the derivative of (3.30) with respect to the error in the state and then assuming that the nominal error is 0 gives

$$\begin{aligned} \frac{d\delta\dot{n}_d}{d\delta X} &= \begin{bmatrix} \frac{d\delta\dot{\bar{n}}_d}{d\delta\bar{q}} & \frac{d\delta\dot{\bar{n}}_d}{d\delta\bar{\omega}} & \frac{d\delta\dot{\bar{n}}_d}{d\delta\bar{n}_d} \end{bmatrix}, && (3.31)\\ &= \begin{bmatrix} 0_{3x3} & [\hat{\bar{n}}_d\times] + [\delta\bar{n}_d\times] & -[\hat{\bar{\omega}}\times] - [\delta\bar{\omega}\times] \end{bmatrix}, && (3.32)\\ &= \begin{bmatrix} 0_{3x3} & [\hat{\bar{n}}_d\times] & -[\hat{\bar{\omega}}\times] \end{bmatrix}. && (3.33) \end{aligned}$$

The state transition model, F, can be found using (3.19), (3.26), and (3.33).

$$F = \begin{bmatrix} -[\hat{\bar{\omega}}\times] & \frac{1}{2}I_{3x3} & 0_{3x3} \\ 0_{3x3} & J^{-1}([J\hat{\bar{\omega}}\times] - [\hat{\bar{\omega}}\times]J) & J^{-1} \\ 0_{3x3} & [\hat{\bar{n}}_d\times] & -[\hat{\bar{\omega}}\times] \end{bmatrix} \tag{3.34}$$

The propagation of the covariance matrix P is found from the state transition model and the process noise via the equation

$$P_{t+1} = \phi P \phi^T + Q_d, \tag{3.35}$$

where $Q_d = GQG^T \Delta t$ and $\phi = e^{F\Delta t}$.

The propagation of the covariance matrix can be tested by using a Monte Carlo method. The results, shown in figs. 3.4, 3.5, and 3.6, indicate that the propagation of the covariance matrix is working correctly because the results from the Monte Carlo simulation are bounded by the expected 3-σ standard deviation.

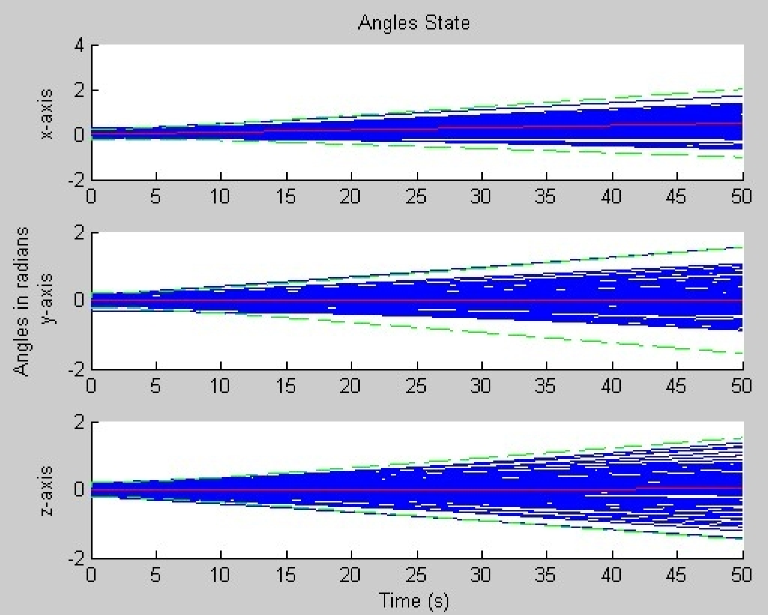

Fig. 3.4: Monte Carlo simulation of the Covariance Propagation of the Quaternion. The results are shown as the euler angles instead of quaternions as they are more intuitive. The red line shows the true state of the angles. The green line shows the predicted boundary using the covariance propagation. The blue lines show the Monte Carlo trials.

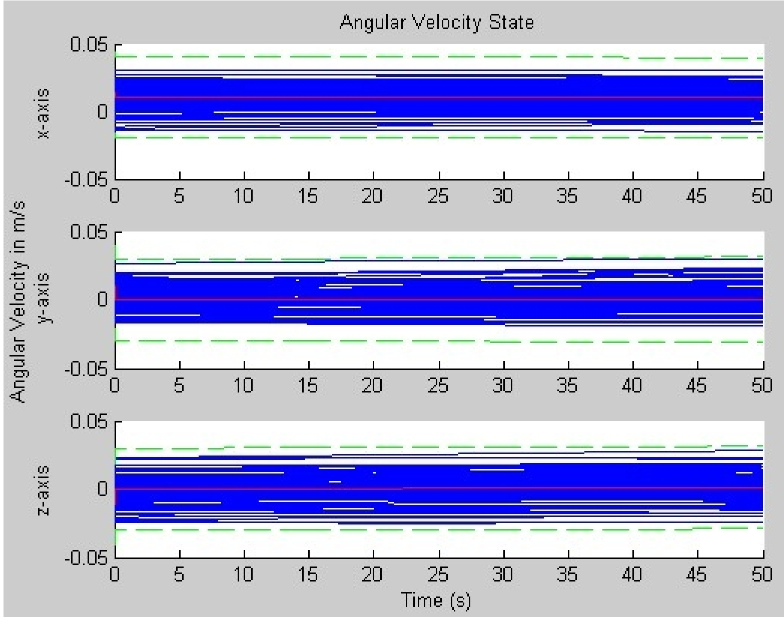

Fig. 3.5: Monte Carlo simulation of the Covariance Propagation of the Quaternion. The red line shows the true state of the angular velocity. The green line shows the predicted boundary using the covariance propagation. The blue lines show the Monte Carlo trials.

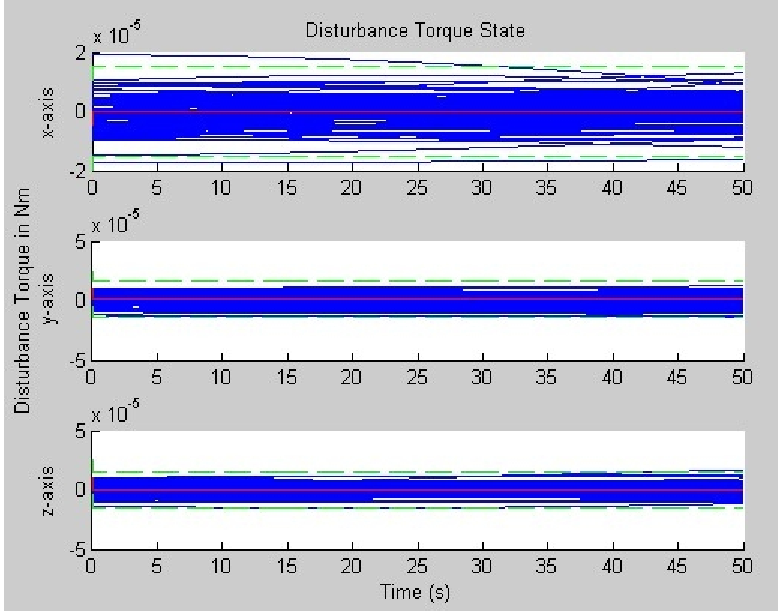

Fig. 3.6: Monte Carlo simulation of the Covariance Propagation of the Quaternion. The red line shows the true state of the torque. The green line shows the predicted boundary using the covariance propagation. The blue lines show the Monte Carlo trials.

3.5 Development of Measurement Model

The only measurement available for the probe is the magnetic field surrounding the spacecraft. This is related to the attitude via the equation

$$b_B = Ab_I, \tag{3.36}$$

where b_B is the magnetic field in body coordinates and b_I is the magnetic field in inertial coordinates. If the linearized equations are used it can be said that

$$b_B = A(\begin{bmatrix} \delta q \\ 1 \end{bmatrix})A(\hat{q})b_I. \tag{3.37}$$

As $\delta\bar{q}$ is the error between the state estimate and the actual state it is expected to be a very small quantity. This allows the use of the approximation that $\delta\bar{q}$ is approximately 1/2 of the Euler Angles [17]. Using the approximation for the rotation matrix in Sidi [12], (3.37) can be written as

$$\begin{aligned} b_B &= (I_{3x3} - 2[\delta\bar{q}\times])A(\hat{q})b_I, &(3.38)\\ &= (I_{3x3} - 2[\delta\bar{q}\times])\hat{b}_B. &(3.39) \end{aligned}$$

Finally, the sensitivity matrix is found by taking the derivative of (3.39) with respect to the state to get

$$\begin{aligned} H &= \begin{bmatrix} \frac{db_B}{d\delta q} & \frac{db_B}{d\delta\omega} & \frac{db_B}{d\delta n_d} \end{bmatrix}, &(3.40)\\ &= \begin{bmatrix} 2[\hat{b}_B\times] & 0_{3x3} & 0_{3x3} \end{bmatrix}. &(3.41) \end{aligned}$$

In order to test the sensitivity matrix it is necessary to check that a change in the state will result in a change in the measurement according to the magnitude and direction calculated by H, the measurement sensitivity matrix. Another Matlab simulation was created to do this and (3.41) was verified to be correct. These results can be seen in fig. 3.7.

3.6 Kalman Filter Verification and Tests

In order to verify the functioning of the Kalman filter derived in the previous section several sets of data were created using the SPAS. For the purpose of verifying the Kalman filter the noise for all elements in the SPAS was set to zero. Noise on the magnetic field measurements was instead done by simple random number generation with a strength of 100 nT. This allowed for the most basic simulation possible so as to understand the limitations of the Kalman filter via the dynamics of the system. The data used a range of initial angular velocities from rates of 0.01 rad/s to 3.14 rad/s on different axis. The initial simulations

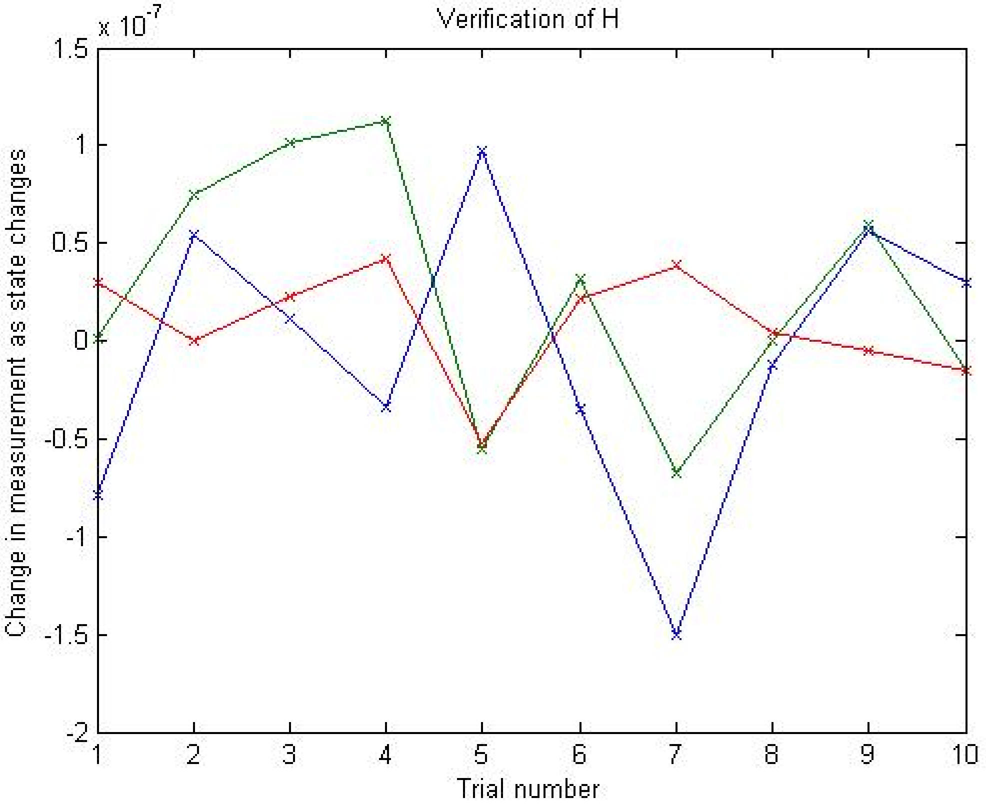

Fig. 3.7: Verification that the sensitivity matrix was derived correctly. The x's show the change in the measurement as the state changes randomly. The line shows what H predicts that change should be.

used a constant torque of 0 on the x and z axis and $1 * 10^{-6}$ Nm on the y axis. The torque was constant in the inertial frame so that as the spacecraft rotated it viewed the torque as rotating. The later simulations used the more realistic torque simulator built into the overall model. Various initial quaternions were used for the simulation as well.

The first simulation run had an initial angular velocity of $\omega_i = \begin{bmatrix} .01 & 0 & 0 \end{bmatrix}^T$, the constant torque, and a quaternion initialized to $q = \begin{bmatrix} 0 & 0 & 0 & 1 \end{bmatrix}^T$. As a result of it being based solely on magnetometer measurements all the states are not observable in this Kalman filter. Figure 3.8 shows that the filter exhibited some difficulty in tracking such a slowly varying system. Later in the section it is shown that some of this problem can be alleviated by using the electric field data.

The second distinct simulation run, used a starting angular velocity of $\omega_i = \begin{bmatrix} .1 & 0 & -0.05 \end{bmatrix}^T$, the same torques, and the same quaternion. This system was able to track much better than the first, although still not to a degree that would allow for accurate attitude determination. The results are shown in fig. 3.9.

Two more distinctly different data sets were tried in testing the original derived Kalman filter. Both of these schemes used the more realistic torques generated by the model itself. It

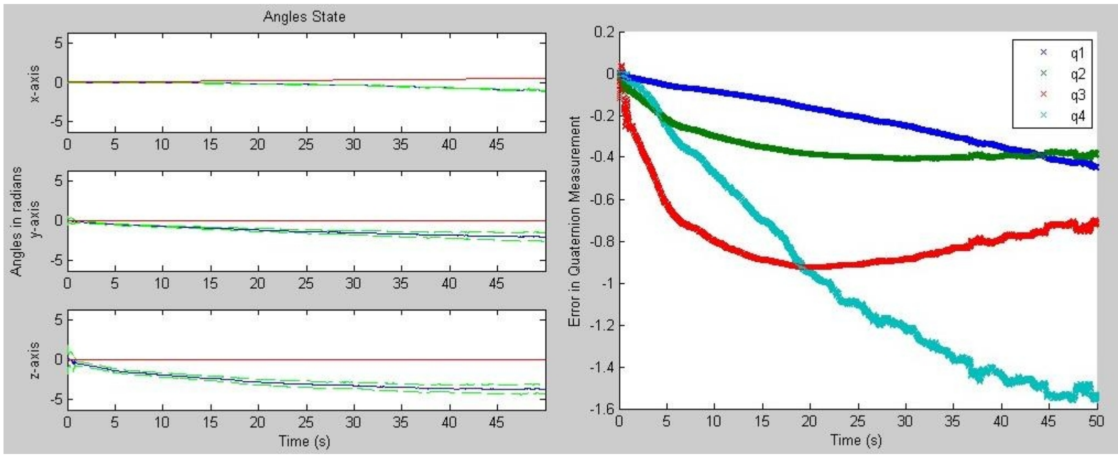

Fig. 3.8: Kalman filter results from the first simulation. The graph on the left shows the true attitude angles for the simulation (red) in comparison to the estimated angles (blue) and the 3-σ deviation (green). The right graph shows the error in the quaternion estimate in comparison to the true quaternions. The red, green, and blue lines are the quaternion vector error; the cyan line is the scalar quaternion error.

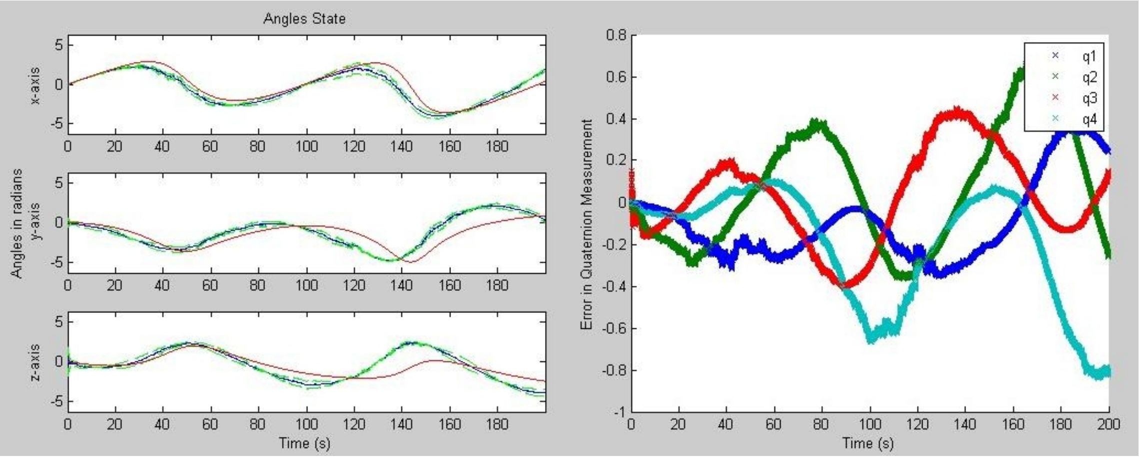

Fig. 3.9: Kalman filter results from the second simulation. The graph on the left shows the true attitude angles for the simulation (red) in comparison to the estimated angles (blue) and the 3-σ deviation (green). The right graph shows the error in the quaternion estimate in comparison to the true quaternions. The red, green, and blue lines are the quaternion vector error; the cyan line is the scalar quaternion error.

was found that for an optimal attitude determination the angular velocity of the spacecraft should be between about .3 rad/s and 1 rad/s. The third simulation used values of $\omega_i = \begin{bmatrix}1 & -0.2 & -0.5\end{bmatrix}^T$ and achieved results with a 3-σ standard deviation of about .01 radians (or around 1/2 degree). This appears to agree with the results demonstrated by Psiaki [16].

At rates greater than this, the filter begins to have a difficult time tracking the data and the standard deviation increases. The fourth simulation, using an initial rate of $\omega_i = \begin{bmatrix}pi/8 & -pi & -pi/4\end{bmatrix}^T$, had a 3-$\sigma$ standard deviation of about 0.08 radians (or 4 degrees). The results from these two simulations can be seen in figs. 3.10 and 3.11.

Following these tests two additional measurements were tested with the Kalman filter. The first extra measurement is the angular velocity as demonstrated by the spin of the magnetometer. As a result of the requirement to spin the spacecraft in order to offset the work function and sheath errors associated with the measurement of the electric field, it is possible to get a rough estimate of the angular velocity of the spacecraft by observing the sinusoidal pattern of the magnetometer measurements. It seems unlikely that the measurement could be more accurate then 0.01 rad/s so that was chosen as the measurement standard deviation. This measurement was added to the Kalman filter and tested with the

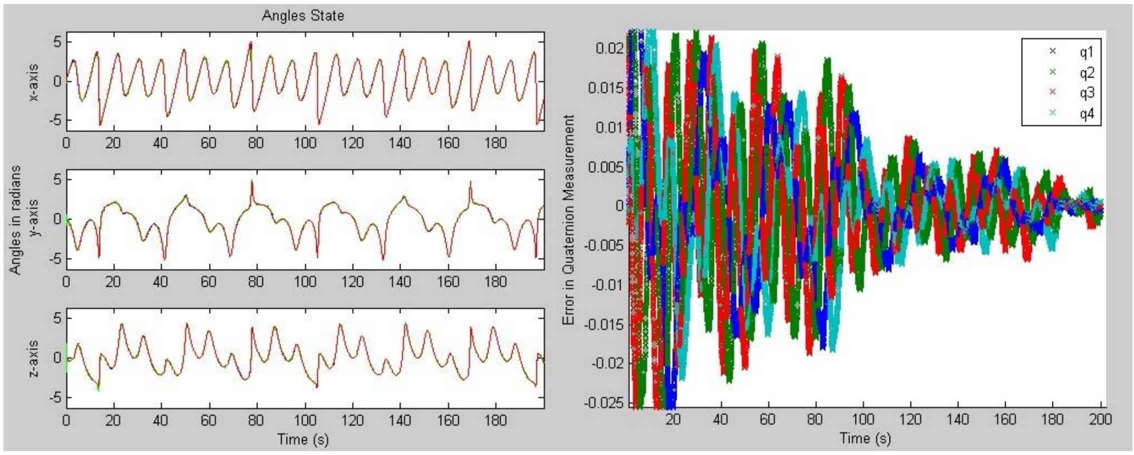

Fig. 3.10: Kalman filter results from the third simulation. The graph on the left shows the true attitude angles for the simulation (red) in comparison to the estimated angles (blue) and the 3-σ deviation (green). The right graph shows the error in the quaternion estimate in comparison to the true quaternions. The red, green, and blue lines are the quaternion vector error; the cyan line is the scalar quaternion error.

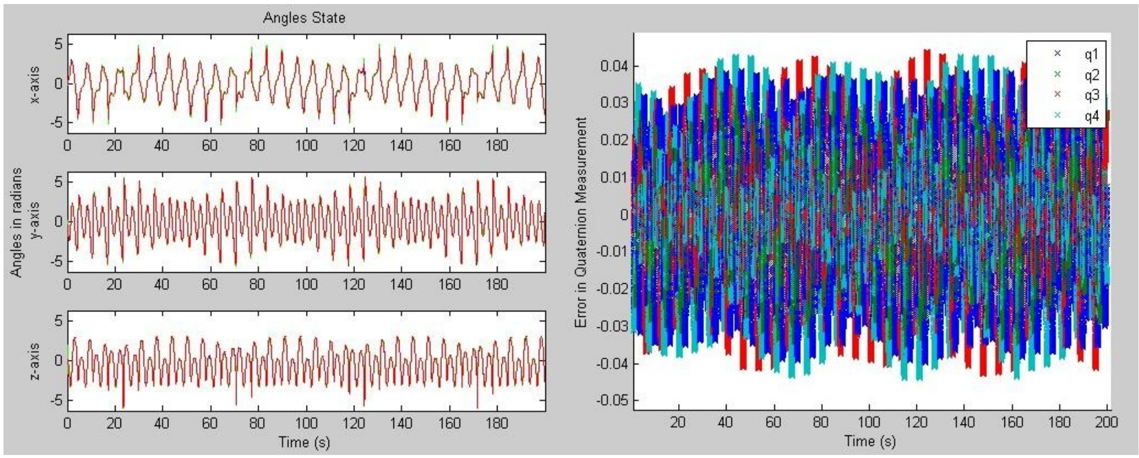

Fig. 3.11: Kalman filter results from the final simulation. The graph on the left shows the true attitude angles for the simulation (red) in comparison to the estimated angles (blue) and the 3-σ deviation (green). The right graph shows the error in the quaternion estimate in comparison to the true quaternions. The red, green, and blue lines are the quaternion vector error; the cyan line is the scalar quaternion error.

second set of simulation data. Unfortunately, as seen in fig. 3.12, this actually corrupted the estimate generated by the Kalman filter. Apparently the inaccuracies in the measurement make it unusable.

The second additional measurement attempted was incorporating the electric field data. As shown in Chapter 2, the electric field data is dominated by the $V \times B$ term existent in the measurement. For this reason, the actual electric field component of the term can be viewed as noise on the assessment of the cross product of the velocity and magnetic field. The sensitivity matrix for this measurement is:

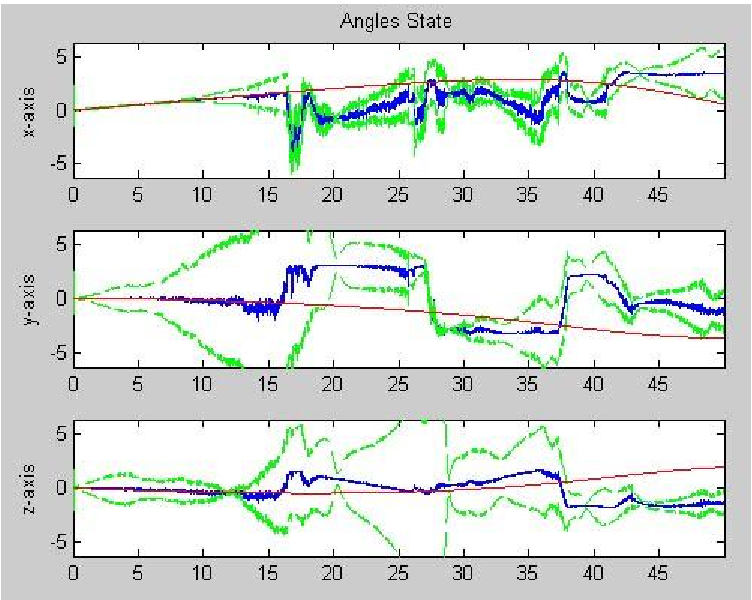

Fig. 3.12: Kalman filter results from the second simulation using angular velocity measurements derived from the magnetic field data. The graph shows the true attitude angles for the simulation (red) in comparison to the estimated angles (blue) and the 3-σ deviation (green).

$$E_B = A(q)V_I \times B_B + \eta, \tag{3.42}$$

$$= V_B \times B_B + \eta, \tag{3.43}$$

$$= A(\delta q)\hat{V}_B \times A(\delta q)\hat{B}_B + \eta, \tag{3.44}$$

$$= (I - 2[\delta q \times])\hat{V}_B \times (I - 2[\delta q \times])\hat{B}_B + \eta, \tag{3.45}$$

$$= (\hat{V}_B + 2[\hat{V}_B \times]\delta q) \times (\hat{B}_B + 2[\hat{B}_B \times]\delta q) + \eta, \tag{3.46}$$

$$= \hat{V}_B \times \hat{B}_B + 2[\hat{V}_B \times][\hat{B}_B \times]\delta q - 2[\hat{B}_B \times][\hat{V}_B \times]\delta q + 4[\hat{V}_B \times]\delta q \times [\hat{B}_B \times]\delta q + \eta, \tag{3.47}$$

$$H = \begin{bmatrix} \frac{dE_B}{d\delta q} & \frac{dE_B}{d\delta \omega} & \frac{dE_B}{d\delta n_d} \end{bmatrix}, \tag{3.48}$$

$$= 2\begin{bmatrix} [\hat{V}_B \times][\hat{B}_B \times] - [\hat{B}_B \times][\hat{V}_B \times] & 0_{3x3} & 0_{3x3} \end{bmatrix}. \tag{3.49}$$

Using this measurement yielded varied results. For the first and second simulation the improvement was remarkable. The extra measurement aids in the observability of the system. So, while this measurement does not work by itself, the results when paired with the magnetic field measurement improve the second simulation's 3-σ standard deviation from 0.6 rad (or 34 degrees) to less than 0.1 rad (about 6 degrees). Unfortunately, the extra measurement did not appear to aid in the problem with the filter tracking the rapidly changing system so that for simulations three and four adding the extra measurement did not improve the results at all. Figures showing the improvement (or lack thereof) can be seen in figs. 3.13 through 3.14.

A summary of the accuracy of the Kalman filter in determining the attitude angles is shown in Table 3.1. The final Kalman filter to be used in the analysis of the STORM payload data includes both magnetic field and electric field measurements.

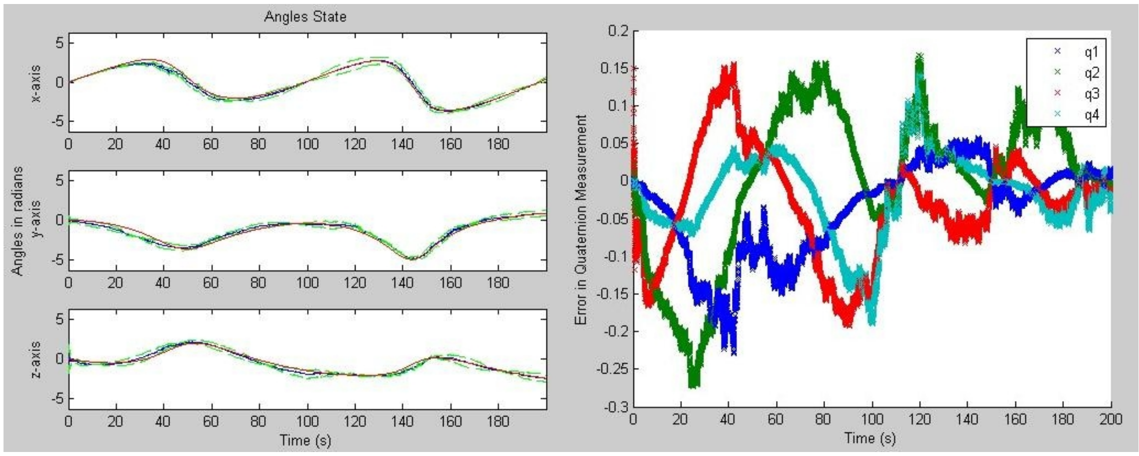

Fig. 3.13: Kalman filter results from the second simulation using simulated electric field data as a measurement. The graph on the left shows the true attitude angles for the simulation (red) in comparison to the estimated angles (blue) and the 3-σ deviation (green). The right graph shows the error in the quaternion estimate in comparison to the true quaternions. The red, green, and blue lines are the quaternion vector error; the cyan line is the scalar quaternion error.

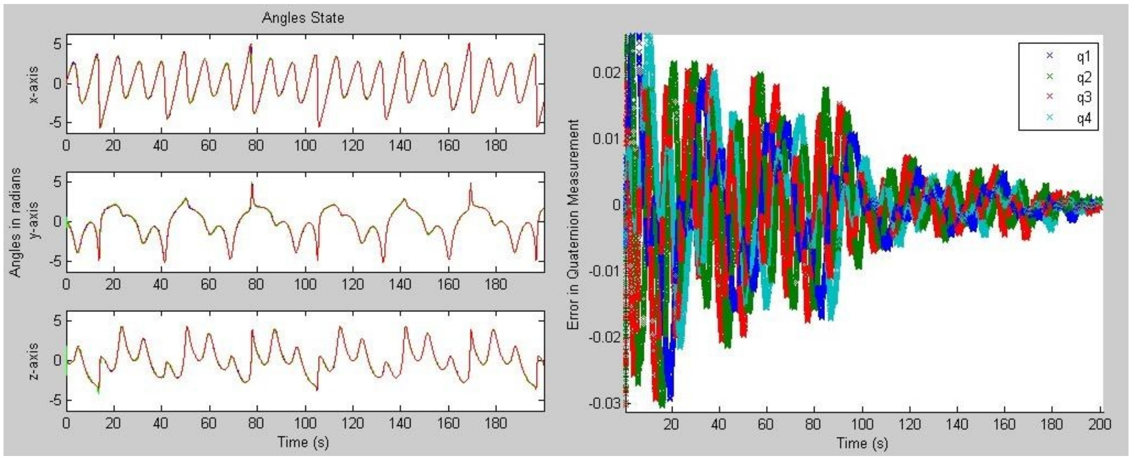

Fig. 3.14: Kalman filter results from the third simulation using simulated electric field data as a measurement. The graph on the left shows the true attitude angles for the simulation (red) in comparison to the estimated angles (blue) and the 3-σ deviation (green). The right graph shows the error in the quaternion estimate in comparison to the true quaternions. The red, green, and blue lines are the quaternion vector error; the cyan line is the scalar quaternion error.

Table 3.1: 3-σ accuracy in degrees of the Kalman filter using either only magnetic field measurements or both magnetic field and electric field measurements. The magnitude of the angular velocity (in m/s) for the simulation is included as it was the determining factor of the end accuracy. Electric field measurements were simulated as 0.005 standard deviation noise on a V×B calculation.

	$\|\omega\|$	Only B Measurement	E and B Measurements
Simulation 1	.010	40	34
Simulation 2	.112	34	6
Simulation 3	1.14	1/2	1/2
Simulation 4	3.26	4	4

Chapter 4

Analysis of the STORMS Payload Data

4.1 Introduction

This chapter is the application of the principles derived in previous sections of this paper. Although formulas may be correct mathematically it is often difficult to implement the same in real-world situations as a result of unpredictable noise, the break down of assumptions, and other such problems. Nevertheless, with careful application, utility can often be found. The main difficulty to be surmounted for the daughter payload data is the fact that the included magnetometer was significantly biased by some magnetic offset. Another challenge, common to all real-world problems, is attempting to understand the accuracies of the result with no truth data to compare against. These challenges, and others, are discussed in the sections below.

4.2 Adjustment of the Magnetometer Data

Unfortunately the magnetometer data shown in fig. 1.3 cannot be assumed to be perfectly representative of the magnetic field through which the spacecraft was flying. All measurement hardware has biases to a greater or lesser degree and despite the effort to identify these biases before launch the environment surrounding the instrument can often effect the bias, meaning that even calibrated data can maintain an unknown bias. The magnetometer onboard the payload of interest is no exception.

To identify the bias present in the magnetometer, a plot of the magnitude of the magnetic field as measured by the magnetometer was created. Although the magnetic field vector was spinning rapidly its magnitude should be changing only gradually and should be nearly equal to the predicted magnitude using the magnetic field model (nearly equal as a result of the fluctuations in the earth's magnetic field). This plot is seen in fig. 4.1.

The results of fig. 4.1 indicate that there is a significant bias on the magnetometer; whether from environmental factors or other onboard hardware it is unknown. This bias makes it much more difficult for the Kalman filter to accurately determine the attitude of the probe. In order to obtain any useful data it must be identified and removed from the measurements.

One possible method for removing the magnetometer bias from the data is to incorporate the bias as one of the states in the Kalman filter. This, however, would add a further level of complexity to an already complex filter and therefore seemed undesirable. Instead, it was decided to determine the bias on the magnetometer data via a nonlinear fit for the magnetic field amplitude to the amplitude suggested by the IGRF model. This would allow the coefficients to be determined and the data adjusted before the use of the Kalman filter.

A simple function to achieve this is built into Matlab. The function *lsqcurvefit* allows a user to find the best set of coefficients that will match one data set to another with a custom function. The function was run looking for both scaling factors and offsets for the

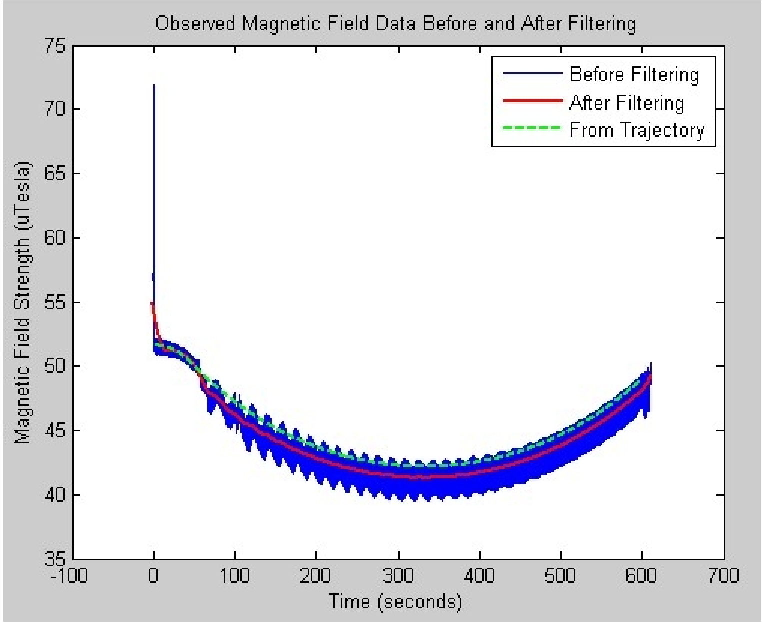

Fig. 4.1: Comparison of the amplitude of the magnetic field. The dotted green line shows the desired amplitude as given by data provided from the IGRF model. The blue line shows the magnetometer. The red line is a filtered version of the magnetometer data.

magnetic field data. The results are shown in Table 4.1. The improvement in the magnetic field amplitude is shown in fig. 4.2.

Although a perfect match was unable to be found (not surprising considering the likelihood that whatever was causing the offset was time varying) the improvement was marked and allowed for an increased performance in the Kalman filter.

4.3 VxB Error Prediction

As shown in Chapter 2, the major error for the final electric field data will be a result of the error in the attitude of the spacecraft. The velocity for the daughter payload is

Table 4.1: Magnetometer bias and scaling coefficients as determined by the Matlab function lsqcurvefit. Bias is in microtesla.

	Scaling	Bias
X-axis	1.0132	1.0889
Y-axis	1.0087	0.1735
Z-axis	1.0257	2.0761

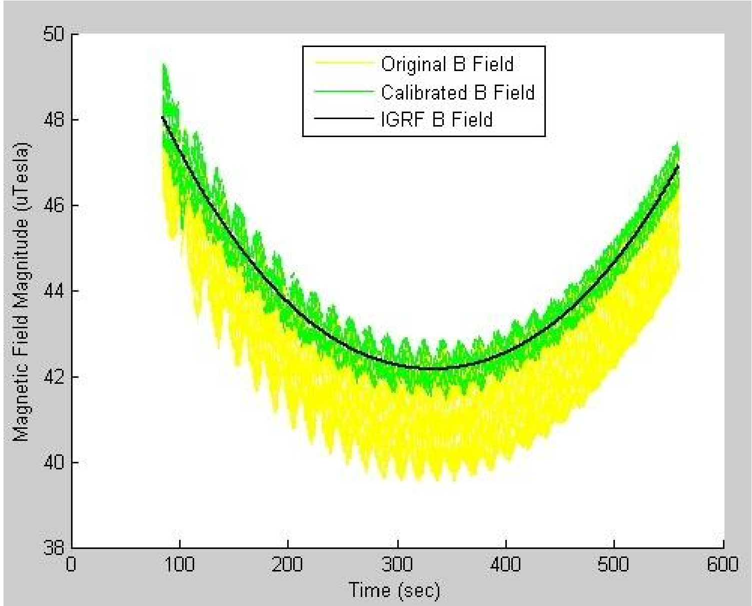

Fig. 4.2: Comparison of the amplitude of the magnetic field before and after bias has been added to to the magnetometer data. The black line shows the desired amplitude as given by data provided from the IGRF model. The yellow line shows the magnetometer data before it is adjusted for the bias. The green line shows the data after it has been adjusted for bias.

significantly different than that of the orbits shown in said chapter so a brief mention of these errors is made here. The analysis for the VxB error was run using the trajectory data provided for the daughter payload in order to understand what attitude would be necessary to achieve a reasonable accuracy for the electric field data. The overall results, shown in figs. 4.3 and 4.4, are encouraging, because they indicate that a much lower order of accuracy is needed than for the example orbits shown. A 1/2 degree accuracy is well within the 10% signal-to-noise margin and even 1 degree would be enough for a good understanding of the electric field data.

4.4 Coordinate System Used

Traditionally, when doing research involved with the magnetic and/or electric field of the earth, the ECEF coordinate system is used for several reasons; the primary reason being that both the magnetic field and electric field of the earth are fixed in this coordinate system (with some variation in time). The use of ECEF, however, causes an invalidation

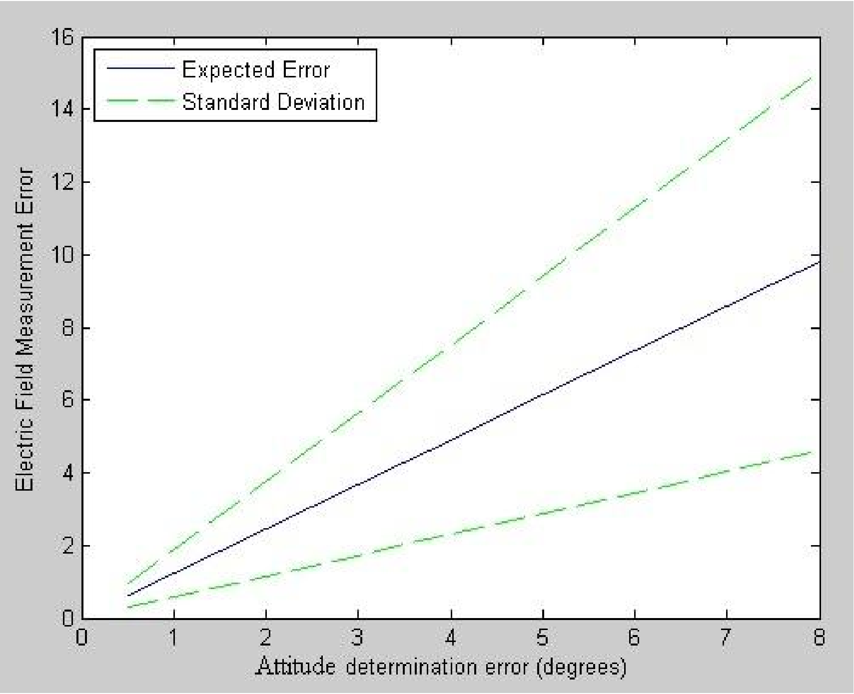

Fig. 4.3: Expected electric field measurement error with the corresponding 3-σ standard deviation for attitude errors varying from 0 to 8 degrees.

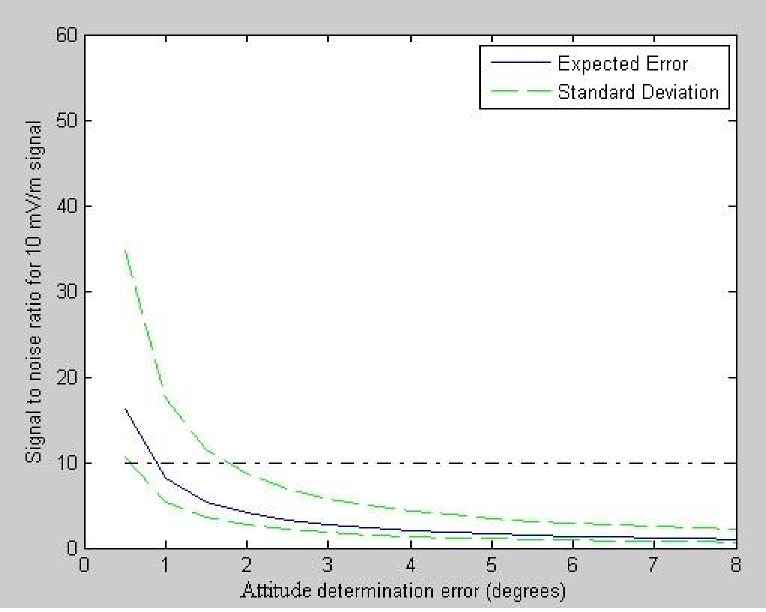

Fig. 4.4: Expected signal-to-noise ratio for the error associated with the velocity induced electric field. The x-axis shows the standard deviation of the attitude error for a specific Monte Carlo analysis. The y-axis is the mean signal-to-noise ratio for each analysis. The green bounds are the standard deviation.

of some of the assumptions made in the derivation of the Kalman filter, in particular those with respect to angular velocity. This is a result of the necessity of including the angular velocity of the earth in the calculation.

In order to avoid the increased complexity of the equations, but at the same time allow for an increased correlation between the results and world magnetic models, a custom coordinate system is used for the results shown in this section. The coordinate system used is an inertial coordinate system related to the J2000 ECI coordinate system by a -101.1061 degree rotation about the z-axis. This aligns the x-axis of the inertial coordinate system with the x-axis of the ECEF system at the start of the collection of data (or 0 seconds on the plots shown).

4.5 Determination of the Attitude of the Spacecraft

In determining the attitude of the spacecraft it is necessary to recognize three different time periods with distinct torques acting on the probe. These different periods can be seen in figs. 1.3 and 1.4. During the first time period, from launch to about 70 seconds, the spacecraft exhibited the desired behavior of nearly stable spinning about the x-axis. At 70 seconds and until 105 seconds there is coning about the x-axis, but it is only to a moderate degree. Following the 105 second mark, and until the end of the flight, the coning seems to become much more intense.

As a result of the distinct nature of these three periods the attitude must be looked at separately to understand what is happening. To do this the measurement residual in the Kalman filter is used. The measurement residual is an indication of how accurate the Kalman filter estimates each measurement. In a system with a standard deviation of five, the Kalman filter should estimate each measurement to within five, or the measurement residual should range from -5 to +5. As no truth data for this system is known, this is the only indication of how well the Kalman filter estimates the system. According to fig. 4.2 the measurement residual should be about 500 nT. Initially, only the magnetometer measurements are used.

The time period from launch to 65.7 seconds consists of the period during which the payload was still connected to the motor and/or the other payload. Also, the booms are not yet deployed. For this reason, the first time period does not contain any useful data for analysis as regards the electric field.

The second time period, from 65.7 to 105 seconds, likely has the best overall attitude estimate. As seen in fig. 4.5, the measurement residual for all of the axes remains close to the 500 nT estimate. This is likely a result of a steady, moderate spin-rate on each of the axes. The attitude estimate during this period should be fairly accurate.

The final time period experiences vast problems in tracking as a result of the unknown disturbance torques acting upon the probe. In fig. 4.6 the residual is seen to be significantly out of the estimated 500 nT boundary. While the x and y axes seem to be close and mostly centered around 0 error as desired, the z-axis is slightly off-center. It seems that this data region would have about half the accuracy of the previous region, although it gets better as time goes on.

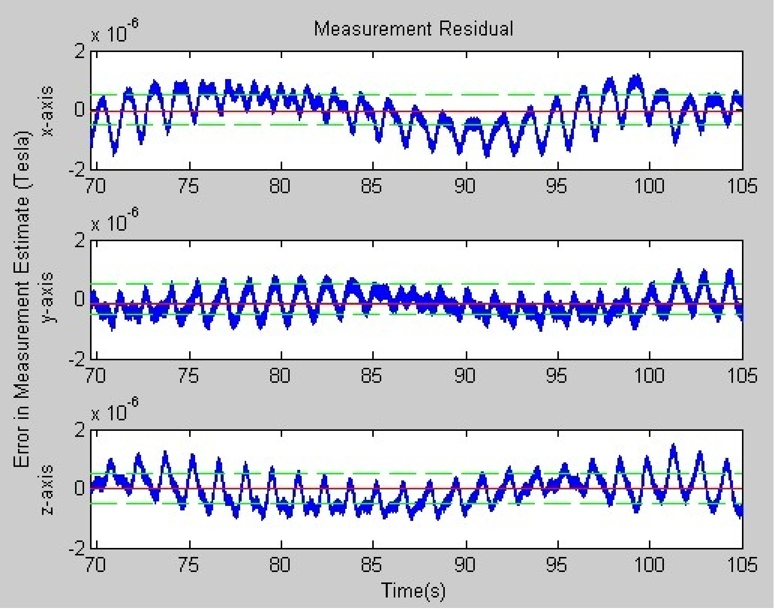

Fig. 4.5: Plot of the measurement residuals from the Kalman filter for the probe data from 70 to 105 seconds. The blue line is the difference between the estimated measurement and the actual measurement. The green line shows the 500 nT boundary for the error. The red line shows the mean (should be 0).

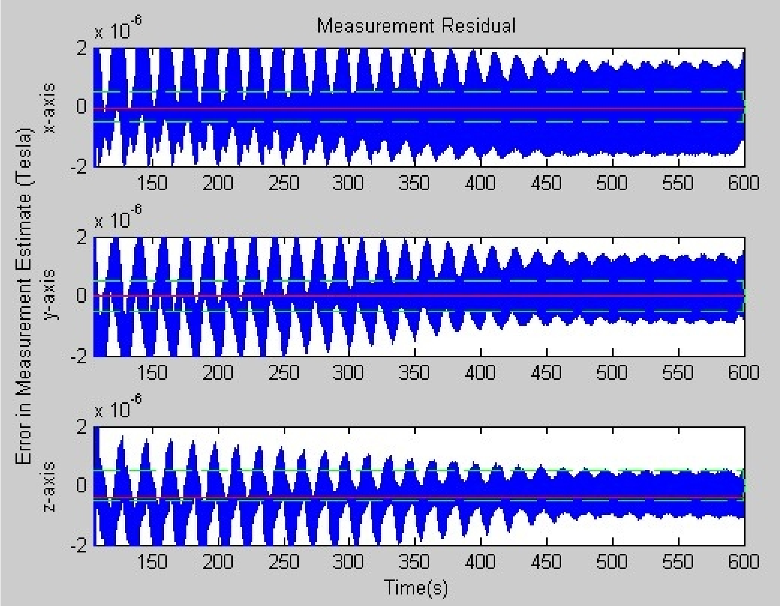

Fig. 4.6: Plot of the measurement residuals from the Kalman filter for the probe data from 105 to 600 seconds. The blue line is the difference between the estimated measurement and the actual measurement. The green line shows the 500 nT boundary for the error. The red line shows the mean (should be 0).

Another indication of the accuracy (or inaccuracy) of the simulation can be seen from the angular momentum determined from the attitude solution. The angular momentum for a spinning spacecraft should be constant and can be found via the formula $h = A(q) * J * \omega$. Using this formula a plot of the angular momentum for the spacecraft was created. It is shown in fig. 4.7. Results were as expected from the graphs of the measurement residuals for the different time periods. While the time from 70 to 105 seconds had the most stable angular momentum it still had some large variation.

In order to determine the level of accuracy that the measurement residuals indicate, the inverse tangent of the error can be used. As mentioned, for the time period from 70 to 105 seconds the measurement of residual was about 1 microtesla. The magnetic field at this point in the flight had a strength of greater than 45 microtesla. This would indicate an accuracy of 1.273 degrees. During the period from 105 seconds to the end of the flight the residual was bounded by the 2 microtesla line. With a magnetic field of not less than 42 microtesla this indicates an accuracy of 2.726 degrees.

To understand what accuracy these numbers are indicative of it is necessary to return

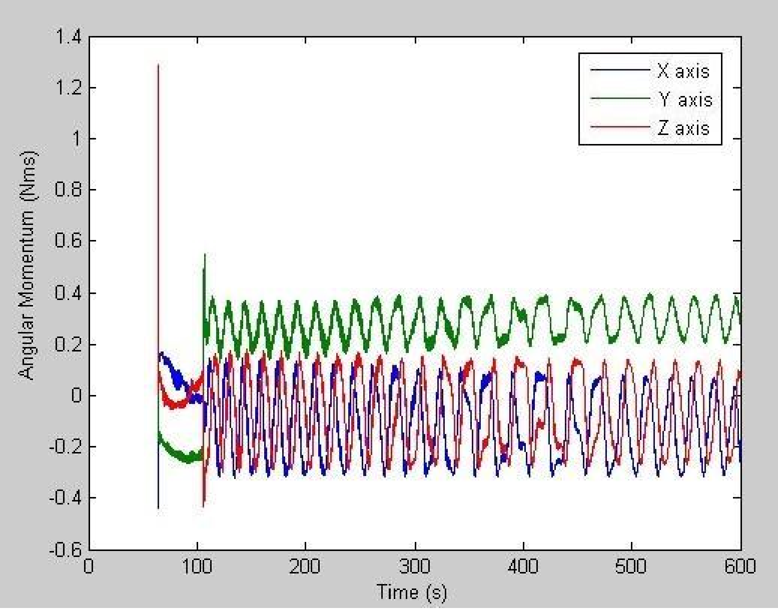

Fig. 4.7: Angular momentum in the inertial coordinate system of the daughter payload as determined by the Kalman filter solution. All three axes are shown.

to the VxB simulation for error. As a result of the widely varying velocity of the daughter payload (from 0.5 km/s to over 2.5 km/s) the mean error shown in fig. 4.4 is only a rough estimate. To have a more accurate picture of the actual errors associated with the results above, figs. 4.8 and 4.9 were created which show the expected error with its 3-σ standard deviation.

4.6 Analysis of the Electric Field Data

The daughter payload on STORMS contained two electric field probes perpendicular to each other. The probes were aligned such that one probe measured the electric field along the body y-axis and the other probe measured the electric field along the body z-axis. Before this data could be used, certain adjustments of the data must be done.

The overall length of the booms was 2.6416 ± 0.127 meters. As shown in sec. 2.2.7, the deviation in the length will result in some error in the measurement. However, also as noted in that section, such a small error in the length of the booms will have a very minimal effect, especially when compared to the likely attitude inaccuracies. Thus, for this data, it

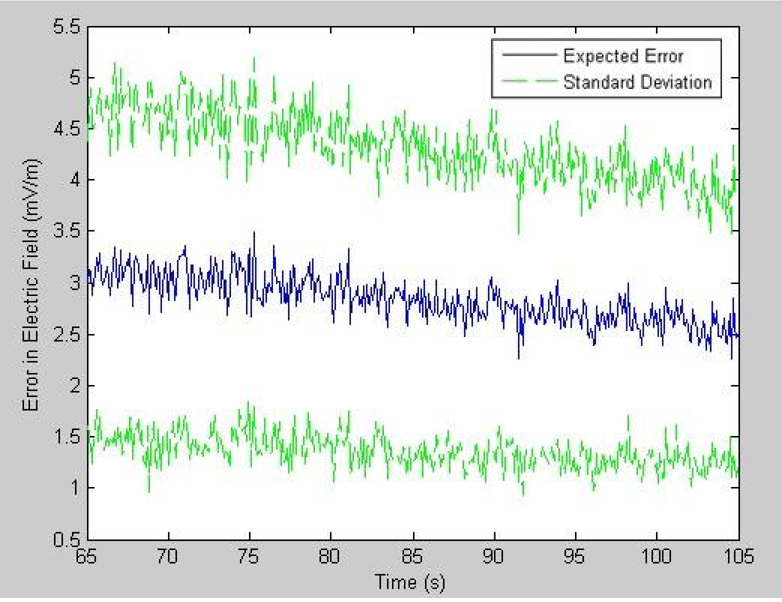

Fig. 4.8: Expected electric field measurement error with the corresponding 3-σ standard deviation for an attitude error of 1.273 degrees over the time 65 to 105 seconds. Time varies across the x-axis in seconds. Electric field error varies across the y-axis in mV/m.

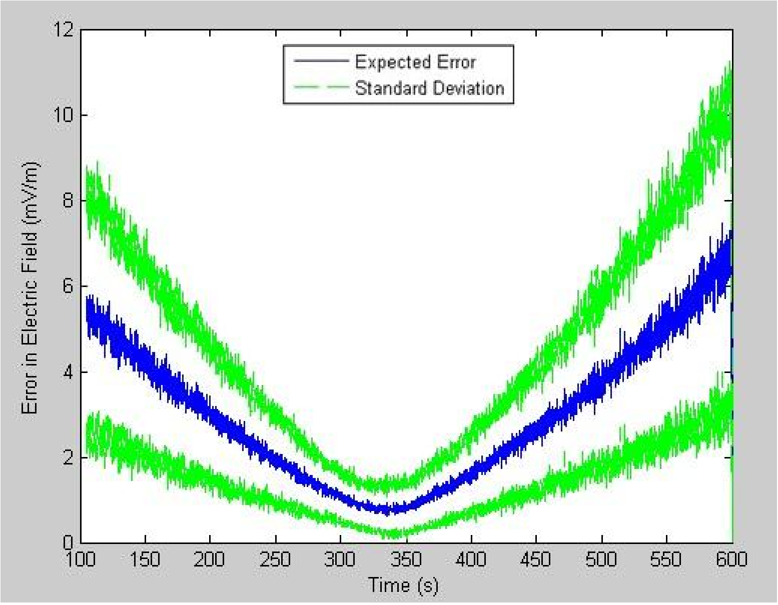

Fig. 4.9: Expected electric field measurement error with the corresponding 3-σ standard deviation for an attitude error of 2.726 degrees over the time 105 to 600 seconds. Time varies across the x-axis in seconds. Electric field error varies across the y-axis in mV/m.

is ignored.

The second error looked at was the sheath and work function errors. These errors can be approximated by the offset of the sinusoidal data allowing them to be removed. In figs. 4.10 and 4.11 the plots of the electric field data for the two probes are shown along with the calculated offset. The offset was calculated by taking the mean of the data at each point within a 2 second range. Both the actual offset and the filtered offset were tested and it was seen that the actual offset gives better results further in the simulation.

Figures 4.12 and 4.13 show the adjusted electric field data. This data was time adjusted by 60 seconds to bring it into alignment with the magnetometer data and the Kalman filter simulation. Anomalous times were removed to improve the accuracy of the Kalman filter run. These times included the initial boom deployment and the unknown disturbance at 105 seconds.

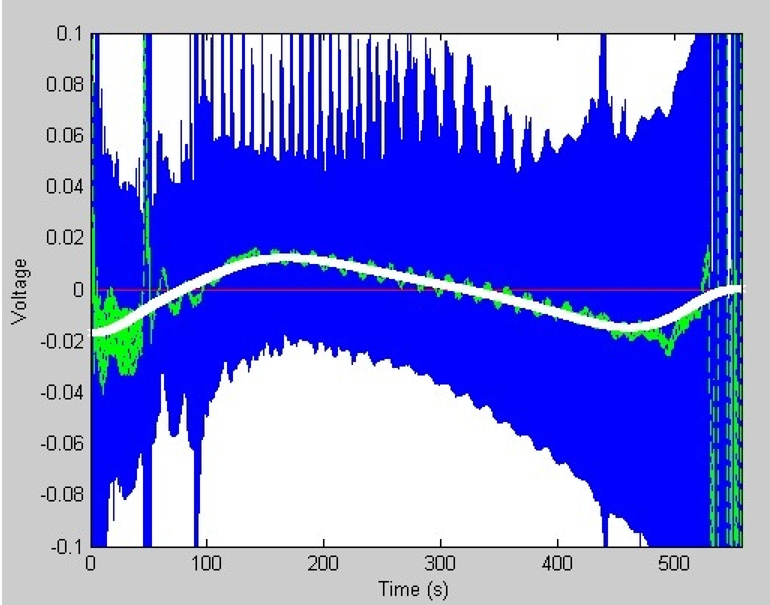

Fig. 4.10: Electric field data along the body y-axis. The blue line is the data. The green line is the calculated offset from zero. The white line is the filtered version of the offset.

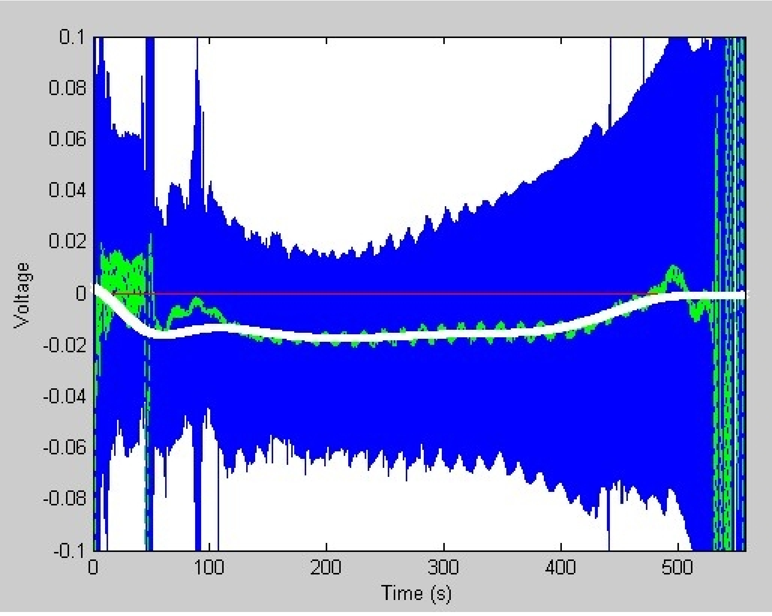

Fig. 4.11: Electric field data along the body z-axis. The blue line is the data. The green line is the calculated offset from zero. The white line is the filtered version of the offset.

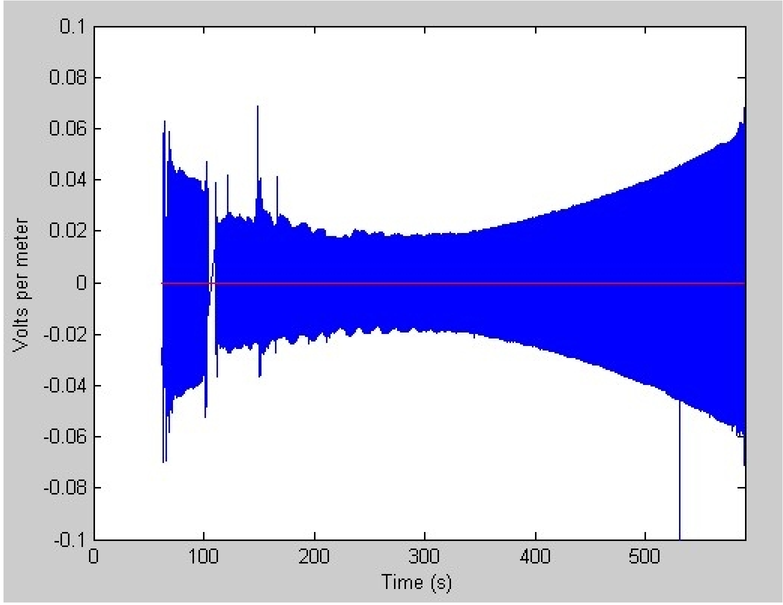

Fig. 4.12: Electric field data along the body y-axis. The blue line is the data. The red line shows zero.

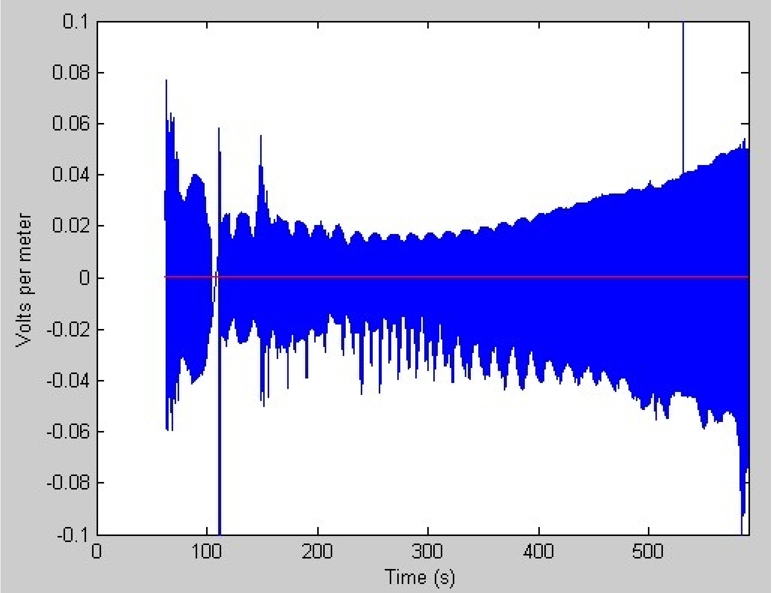

Fig. 4.13: Electric field data along the body z-axis. The blue line is the data. The red line shows zero.

The results using the electric field data were varied. The electric field data from probes 2 and 4 seemed to be much more noisy than that of probes 1 and 3. Thus, the inclusion of this data did nothing to aid in the simulation. However, the inclusion of the data from probes 1 and 3 seemed to increase the accuracy of the Kalman filter results. Although this increase was not greatly reflected in the measurement residuals, the angular momentum increased quite markedly in stability; particularly during the time period from 65 to 105 seconds. Plots showing the angular momentum for the simulation which included the y-axis electric field data can be seen in figs. 4.14 and 4.15. Also included is an image of the angle between the body x-axis and the angular momentum vector in fig. 4.16. For the system, this angle should be constant or at least varying little. This again demonstrates that the Kalman filter is not quite able to lock onto the correct attitude of the probe.

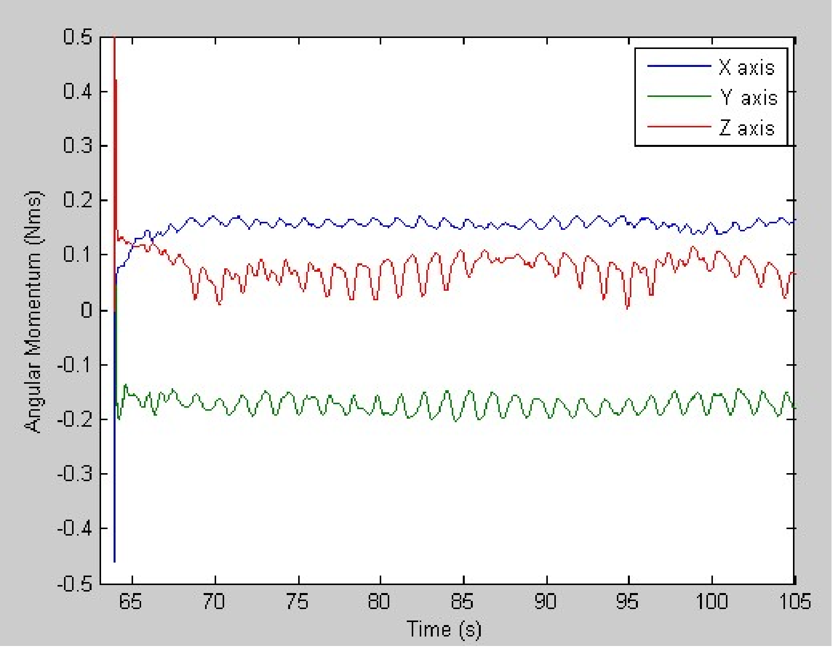

Fig. 4.14: Angular momentum in the inertial coordinate system of the daughter payload as determined by the Kalman filter solution before the disturbance at 105 seconds. The figure shows the results when the y-axis electric field data is included in the analysis.

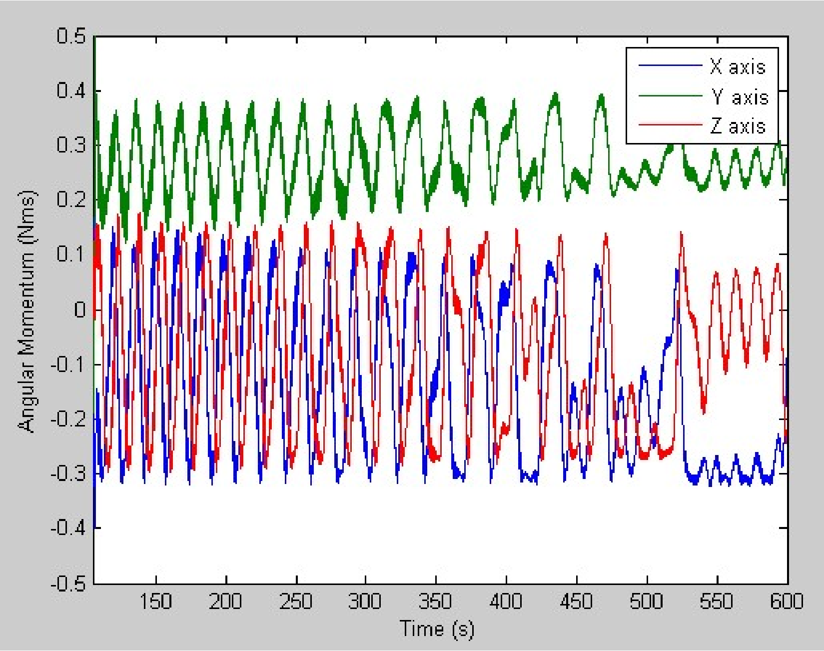

Fig. 4.15: Angular momentum in the inertial coordinate system of the daughter payload as determined by the Kalman filter solution after the disturbance at 105 seconds. The figure shows the results when the y-axis electric field data is included in the analysis.

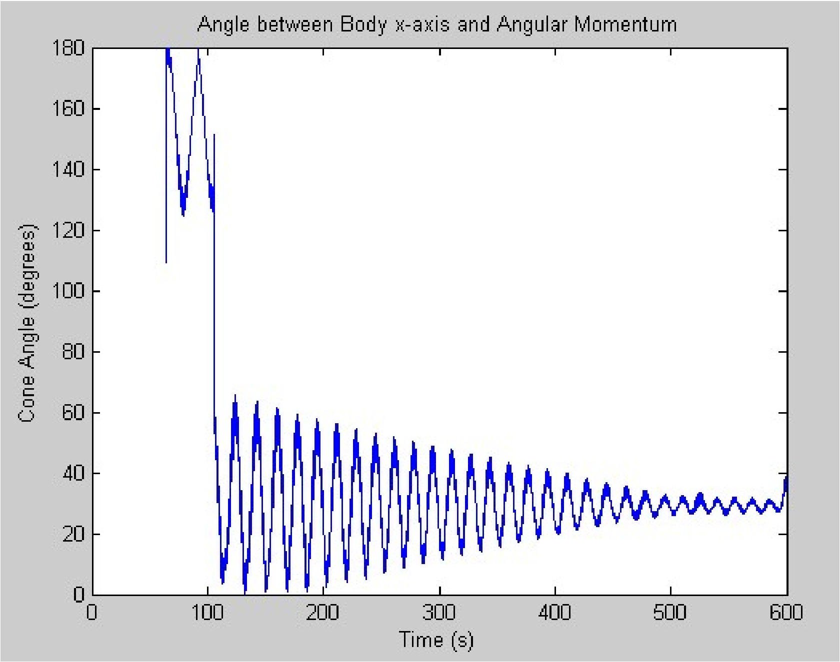

Fig. 4.16: Angle between the angular momentum in the inertial coordinate system of the daughter payload and the body x-axis of the daughter payload as determined by the Kalman filter solution. The figure shows the results when the y-axis electric field data is included in the analysis.

Chapter 5

Conclusion

As stated in the introduction, one of the initial purposes of this project was to determine the viability of the data collected by the daughter payload on the STORMS mission. According to the findings of this thesis it would appear that the electric field data is usable to a rough degree between the time that the daughter payload was released from the mother payload, and the unknown event at approximately 105 seconds. The electric field data during this period has an expected error of 3.5 mV/m. The data following this period has a larger error but still contains some useful, rough data.

It appears from the behavior of much of the data analyzed during this paper that one of the booms (most likely the boom connected to probe 2) was broken or damaged during whatever event happened at 105 seconds. The evidence for this comes primarily from two sources. First, the resulting angular momentum seems to indicate that some sort of energy dissipation was occurring. Although the damaged boom was held rigid by the centrifugal force of the payload there would have been some energy slowly lost. Second, the resulting z-axis data from probes 2 and 4 is significantly more noisy than the data from probes 1 and 3 with several anomalous spikes.

The other stated purposes of this paper have met with some success. The Kalman filter derived, could be of use to spacecraft with only magnetometer measurements for attitude determination and its ability, in particular, to use electric field data collected concurrently increasing its usefulness. Also, some of the limits of attitude determination using only magnetometers have been explored.

Finally, the chapter on errors associated with electric field probes is of importance for planning future missions, such that the requirements of the mission in many different aspects regarding the collection of the electric field are better understood. This will allow for more successful missions in the future that can provide valuable answers to questions regarding the electric field of the earth.

References

[1] J. Gregory, “Design and calibration of the Utah State University floating potential probe,” Master’s thesis, Utah State University, Logan, 2007.

[2] High Frequency Active Auroral Research Program, “About the ionoshpere,” [http://www.haarp.alaska.edu/haarp/ion1.html], 2007.

[3] Wikipedia, “Ionosphere,” [http://en.wikipedia.org/wiki/Ionosphere], 2009.

[4] Geophysics Study Committee, Geophysics Research Forum, *The Earth’s Electrical Environment*, pp. 195–205. Washington, DC: National Academies Press, 1986.

[5] M. E. Disbrow, “Postflight mission analysis terrier mk70-black brant 36.218 ue,” prepared for NASA Goddard Space Flight Center, Apr. 2008.

[6] A. Piel, M. Hirt, and C. T. Steigies, “Plasma diagnostics with langmuir probes in the equatorial ionosphere: I. The influence of surface contamination,” *Journal of Physics D: Applied Physics*, vol. 34, pp. 2643–2649, 2001.

[7] W. E. Amatucci, P. W. Schuck, D. N. Walker, P. M. Kintner, S. Powell, B. Holback, and D. Leonhardt, “Contamination-free sounding rocket langmuir probe,” *Review of Scientific Instruments*, vol. 72, pp. 2052–2057, 2001.

[8] C. Swenson, “Electric field double probes,” in *ECE 7210 Spacecraft Instrumentation Course Notes*, 2009.

[9] C. Swenson, “Collection currents,” in *ECE 7210 Spacecraft Instrumentation Course Notes*, 2009.

[10] U. Fahleson, “Theory of electric field measurements conducted in the magnetosphere with electric probes,” *Space Science Reviews*, vol. 7, pp. 238–261, 1967.

[11] J. B. Camp, T. W. Darling, and R. E. Brown, “Macroscopic variations of surface potentials of conductors,” *Journal of Applied Physics*, vol. 69, pp. 7126–7129, 1991.

[12] M. J. Sidi, *Spacecraft Dynamics and Control.* New York: Cambridge University Press, 1997.

[13] T. Humphreys, “Attitude determination for small satellites with modest pointing constraints,” Master’s thesis, Utah State University, Logan, 2003.

[14] T. Humphreys, M. Psiaki, E. Klatt, S. Powell, and P. Kintner, “Magnetomter-based attitude and rate estimation for a spacecraft with wire booms,” *Journal of Guidance, Control, and Dynamics*, vol. 28, pp. 584–593, 2005.

[15] M. L. Psiaki, “Global magnetomater-based spacecraft attitude and rate estimation,” *Journal of Guidance, Control, and Dynamics*, vol. 27, pp. 240–249, 2004.

[16] M. L. Psiaki, "Three-axis attitude determination via kalman filtering of magnetometer data," *Journal of Guidance, Control, and Dynamics*, vol. 13, pp. 506–513, 1990.

[17] J. L. Crassidis and J. L. Junkins, *Optimal Estimation of Dynamic Systems.* Washington, DC: Chapman and Hall/CRC, 2004.

Appendices

Appendix A

Electric Field Measurement Error Tests

This appendix is on the included CD. It contains code for calculating the various errors associated with electric field measurement instruments. The main included files and their purposes are as follows:

booms.m -	Calculates the error in the electric field associated with boom length errors and misalignments.
resistivity.m -	Calculates the error in the electric field associated with the resistance of the instrument and the resistance of the plasma sheath.
sheath.m -	Calculates the error in the electric field associated with variances in the plasma sheath surrounding the probes.
VxB.m -	Calculates the error in the electric field associated with uncertainties in the magnitude of the velocity and magnetic field.
VxBatt.m -	Calculates the error in the electric field associated with uncertainties in the attitude of the spacecraft.
work.m -	Calculates the error in the electric field associated with the work function of the probes.

Appendix B

Magnetic Field Comparison Code

This appendix is on the included CD. It contains code used to compare the magnitude of the measured magnetic field with the magnitude of the magnetic field as calculated from the trajectory data. This data is then used to adjust the measured magnetometer data in order to increase the accuracy of the measurements.

Appendix C

Kalman Filter Code

This appendix is on the included CD. The code contained in this appendix is the Kalman filter for determining the attitude of a spacecraft based upon magnetometer data. The main files and folders in this appendix are:

data -	Folder containing all of the necessary data tests and test data for the Kalman filter.
testfunctions -	Various functions used to determine the accuracy and functioning of the Kalman filter.
utilities -	Various functions necessary to the Kalman filter code.
Kalman_main.m -	Kalman filter for use with the test data, either with or without electric field data.
Kalman_main2.m -	Kalman filter for use with the STORMS daughter payload data; does not use the electric field.
Kalman_main3.m -	Kalman filter for use with the STORMS daughter payload data; includes the electric field measurements in the Kalman filter to increase performance.

Appendix D

SDL Pearl ADCS Simulation Code

This appendix is on the included CD. It contains the SDL Pearl ADCS simulation code used to generate test data for the Kalman filter.